TECHNICKÁ UNIVERZITA V LIBERCI
Fakulta strojní

Experimental Investigation of the Wake behind the Bluff Body with Heating

Diplomová práce

Studijní program: N2301 – Mechanical Engineering
Studijní obor: 2302T010 – Machines and Equipment Design

Autor práce: **Narendar Padmanaban**
Vedoucí práce: Ing. Petra Dančová, Ph.D.

Liberec 2019

TECHNICAL UNIVERSITY OF LIBEREC
Faculty of Mechanical Engineering

Experimental Investigation of the Wake behind the Bluff Body with Heating

Master thesis

Study programme: N2301 – Mechanical Engineering
Study branch: 2302T010 – Machines and Equipment Design

Author: **Narendar Padmanaban**
Supervisor: Ing. Petra Dančová, Ph.D.

Liberec 2019

TECHNICAL UNIVERSITY OF LIBEREC
Faculty of Mechanical Engineering

Master Thesis Assignment Form

Experimental Investigation of the Wake behind the Bluff Body with Heating

Name and Surname: **Narendar Padmanaban**
Identification Number: S17000402
Study Programme: N2301 Mechanical Engineering
Specialisation: Machines and Equipment Design
Assigning Department: Department of Power Engineering Equipment
Academic Year: **2018/2019**

Rules for Elaboration:

This thesis deals with the experimental investigation of the wake created behind the bluff body in water as a working fluid. The PIV and pLIF methods are used.

1. Make the "state of art" of the problem.
2. Design the experimental setup.
3. Design the heater of the bluff body.
4. Perform the experiments of the velocity fields using PIV method.
5. Perform the experiments of the temperature fields using pLIF method.
6. Analyze your data and do the comparison with the literature.

Scope of Report:	up to 50 pages
Thesis Form:	printed
Thesis Language:	English

List of Specialised Literature:

[1] WIENEKE, Bernhard. PIV Uncertainty Quantification and Beyond. *Unpublished* [online]. 2017 [vid. 2019-04-25]. Dostupné z: doi:10.13140/rg.2.2.26244.42886

[2] KINSEY, J L. Laser-Induced Fluorescence. *Annual Review of Physical Chemistry* [online]. 1977, 28(1), 349-372. ISSN 0066-426X, 1545-1593. Dostupné z: doi:10.1146/annurev.pc.28.100177.002025

Thesis Supervisor:	Ing. Petra Dančová, Ph.D. Department of Power Engineering Equipment
Date of Thesis Assignment:	1 November 2018
Date of Thesis Submission:	30 April 2020

Technická univerzita v Liberci
L. S.
-8-

prof. Dr. Ing. Petr Lenfeld
Dean

Liberec 1 February 2019

doc. Ing. Václav Dvořák, Ph.D.
Head of Department

Declaration

I hereby certify I have been informed that my master thesis is fully governed by Act No. 121/2000 Coll., the Copyright Act, in particular Article 60 – School Work.

I acknowledge that the Technical University of Liberec (TUL) does not infringe my copyrights by using my master thesis for the TUL's internal purposes.

I am aware of my obligation to inform the TUL on having used or gran- ted license to use the results of my master thesis; in such a case the TUL may require reimbursement of the costs incurred for creating the result up to their actual amount.

I have written my master thesis myself using the literature listed below and consulting it with my thesis supervisor and my tutor.

At the same time, I honestly declare that the texts of the printed ver- sion of my master thesis and of the electronic version uploaded into the IS STAG are identical.

26. 4. 2019 Narendar Padmanaban

ACKNOWLEDGEMENT

I take this chance to express my deep sense of gratitude to the University, TECHNICAL UNIVERSITY OF LIBEREC for providing an excellent infrastructure, lab facilities and support to pursue my thesis work.

My sincere thanks to my supervisor Ing. PETRA DANČOVÁ, Ph.D., who, inspite of having practically no spare time, still managed to find some time to provide me help and valuable advices during the whole journey of my thesis.

I extend my special thanks to Ing. JAROSLAV PULEC for his guidance, supervision and support throughout the execution of thesis.

Finally I thank my family and friends for being helpful and supportive throughout my studies.

This publication was written at the Technical University of Liberec as part of the project "Experimental, theoretical and numerical research in fluid mechanics and thermodynamics, no.21291" with the support of the Specific University Research Grant, as provided by the Ministry of Education, Youth and Sports of the Czech Republic in the year 2019.

THEME: EXPERIMENTAL INVESTIGATION OF THE WAKE BEHIND THE BLUFF BODY WITH HEATING

ABSTRACT:

Wake behind heated cylinder have been experimentally investigated at low Reynolds numbers. The electrically heated cylinder is mounted in a horizontal circulation water channel facility. The dimensionless parameter Reynolds number is varied to examine flow behavior by forced convection experimental condition. Particle Image Velocimetry (PIV) and Planar-Laser Induced Fluorescence methods (PLIF/LIF) has been used for flow visualization and analysis of the flow structures. The complete vortex-shedding sequence has been recorded using a high speed camera. The dynamical characteristics of the vertical structures – their size, shape and phase are reported. On heating, the changes in the organized structures with respect to shape, size, and their movement are readily perceived from the instantaneous camera images before they reduce to a steady plume.

Keywords: Wake, Heated cylinder, Reynolds number, PIV, LIF

CONTENTS

LIST OF FIGURES

LIST OF TABLES

LIST OF SYMBOLS USED

Re	Reynolds number (1)
Ri	Richardson number (1)
δ	Boundary layer thickness (mm)
U_∞	Free stream velocity of water (m/s)
Δx	Partial image displacement (m)
u	Instantaneous velocity field (m/s)
Δu	Instantaneous velocity (m/s)
u_p	Particle velocity (m/s)
u_f	Fluid velocity (m/s)
f_c	Cut-off frequency (Hz)
υ	Kinematic viscosity (m^2/s)
ρ_f	Density of the fluid – water (kg/m^3)
d_p	Diameter of the seeding particle (μm)
ρ_p	Density of the seeding particle (kg/mm^3)
τ_p	Relaxation time (s)
ω	Angular frequency (rad/s)
S_ε	Stokes number (1)
λ	Laser light wavelength (nm)
I_1	Light Intensity (W/m^2)
dI	Intensity change (W/m^2)
$\mathcal{F}$	Fourier transforms
Δt	Time delay (s)
dV	Volume (m^3)
dA	Cross sectional area (m^2)
λ_{abs}	Peak absorption wavelength (nm)
λ_{abs}	Emission wavelengths (nm)
L	Length of the circulation channel (mm)

H	Height of the circulation channel (mm)
W	Width of the circulation channel (mm)
D	Diameter or circular cylinder (mm)
T_∞	Ambient Temperature (K)
T_{ref}	Reference Temperature (K)
V	Velocity of the circulating flow (m/s)
μ	Dynamic viscosity (Pa.s)
I_{sat}	Saturation intensity for the dye (W/m^2)
Q	Circulation water flow rate (l/min)
$\in$	Absorption coefficient (1)
Gr	Grashof number (1)

1 INTRODUCTION

The main objective of this thesis is to get a better understanding of the wake behavior of a circular cylinder when the cylinder is heated. The set up is for a case at relatively low speeds, the Reynolds number is set to 300. Flows with Reynolds number varying from 300 to 800 over unheated cylinder have been calculated, and the differences are investigated. These differences are then compared to the changes of the wake when the cylinder is heated in the flow at the same Reynolds number. The working medium is water.

The Experimental investigation of the wake flow behind a heated cylinder operating in forced and mixed convection regime are performed in the present study. The experiments were conducted in a horizontal water channel with the heated cylinder placed horizontally and the flow approaching the cylinder sideward. During the experiments, the Reynolds number and temperature of the approach flow were held constant. By adjusting the surface temperature of the heated cylinder, resulting in a change in the heat transfer process from forced convection to mixed convection. Particle Image Velocimetry (PIV), Planar-Laser Induced Fluorescence (p-LIF) was used for qualitative flow visualization of thermally induced flow structures and quantitative, simultaneous measurements of flow velocity and temperature distributions in the wake of the heated cylinder

Extensive advancement has been made during the most recent decades in both experimental and numerical procedures for the examination of fluid flows. On the experimental side, there has been a general development from intrusive single point estimations to nonintrusive planar estimations, for example, PIV (see, e.g.,[1], [2]) and all the more as of late even time-resolved volume estimations. Concerning computational fluid dynamics (CFD), increments in computer control have permitted the decrease of discretization blunders through calculation on progressively fine frameworks, with the end goal that the prevailing error source remaining stems from the assumptions met in the fundamental physical models, especially for the treatment of turbulence. In this field, a latest hybrid method known as detached eddy simulation (DES) has been appeared to be especially encouraging for bluff-body flows [3].

By varying the Reynolds number, an assortment of flow patterns and vortex shedding characteristics in the wakes of circular cylinders have already been observed. Broad surveys about the impact of Reynolds number on the flow pattern in the wake of an unheated circular cylinder have been given by Roshko [4], Berger and Wille [5], Oertel [6], Williamson [7] and

Zdravkovich [8]. As depicted in the textbook of Incropera and Dewitt [9], heat exchange from a heated cylinder to the encompassing fluid can be either forced convection, mixed convection or pure free convection, contingent upon the proportion between the thermally induced buoyancy force and inertial force, portrayed by the Richardson number ($Ri = Gr/Re^2$, where Gr is the Grashof number and Re is the Reynolds number). [10]

1.1 BLUFF BODY

A bluff body can be characterized as a body that, because of its shape, has separated flow over a considerable part of its surface. Any body which kept in fluid flow, the fluid does not contact the entire limit of the object. An imperative component of a bluff body is that there is an extremely strong collaboration between the viscous and inviscid regions.

At the point when the flow separates from the surface and the wake is formed, the pressure recovery isn't complete. The larger the wake, the smaller is the pressure recovery and the more prominent the pressure drag. The craft of streamlining a body lies, therefore, in molding its form with the goal that partition, and subsequently the wake, is disposed of, or atleast in restricting the separation to a small real part of the body and, consequently, keeping the wake as small as could be expected under the circumstances. Such bodies are known as bluff and a significant pressure drag is related with it.

Cylinders and spheres are referred as bluff bodies because at large Reynolds number the drag is dominated by the pressure losses in the wake.

Therefore, when the drag is dominated by a frictional part, the body is known as streamlined body; while on account of predominant pressure drag, the body is known as bluff body.

A body is said to be streamlined if a conscious effort is made to align its shape with the foreseen streamlines in the flow. Streamline bodies, for example, race cars and airplanes appear to be contoured and smooth. Or else, a body (such as a building) tends to block the flow is said to be bluff or blunt. Normally it is a lot simpler to drive a streamlined body through a liquid, and in this manner streamlining has been of incredible significance in the structure of vehicles and airplanes [11].

The aerodynamic design of cars has advanced from the 1920s as far as possible of the twentieth century. This adjustment in structure from a blunt body to a more streamlined body diminished the drag coefficient from about 0.95 to 0.30 [12].

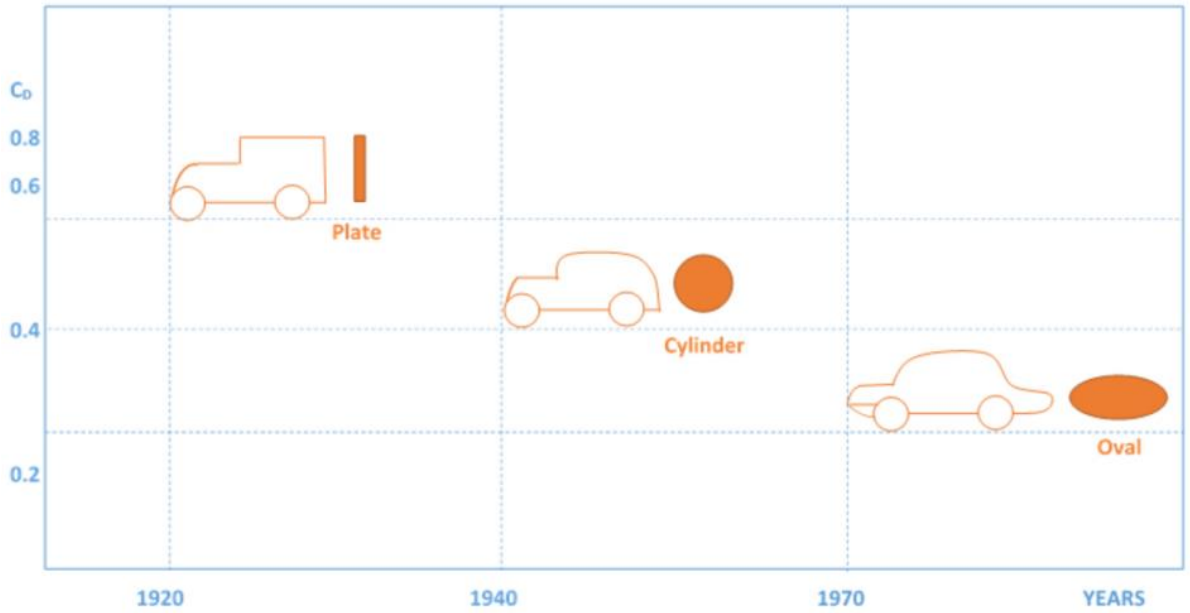

Fig. 1.1 Time history of cars' aerodynamic drag in contrast with change in geometry of streamlined bodies (blunt to streamline) [12]**.**

2 LITERATURE

2.1 ILLUSTRATIONS OF FLOW PAST CYLINDERS

Case I: Circular cylinder without circulation (Stationary cylinder)

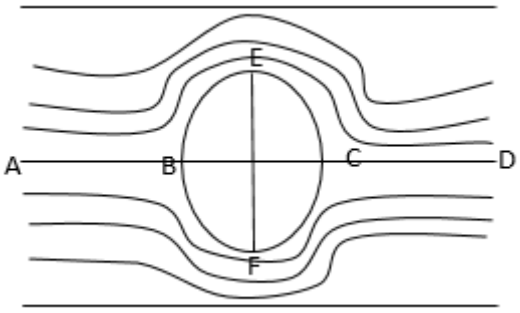

Fig. 2.1 Stationary cylinder experiencing airflow

Consider the flow of air passed an infinite circular cylinder kept in the uniform stream of air (Air is considered to be an ideal fluid)

Observations:

1. The line ABCD together with the circle itself is a streamline called as dividing stream line.
2. The points B & C are the stagnation points.
3. The flow pattern above and below the cylinder surface is identical.
4. The stream lines are symmetrical about the horizontal axis i.e. BC which implies that the velocity distribution and hence the pressure distribution are also symmetrical about the horizontal axis from the continuity and Bernoulli's. Therefore there will be no force in the vertical direction i.e. LIFT IS ZERO.
5. The stream line pattern is also symmetrical about the vertical axis which represents that there is no force in the horizontal direction also i.e. DRAG IS ZERO.

Case-II: Circular cylinder with circulation (Rotating cylinder)

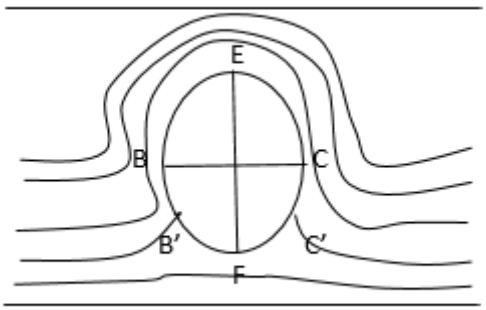

Fig. 2.2 Rotating cylinder experiencing airflow

The circulation is incorporated by a rotating the cylinder with the help of some external source.

Observations:

1. The stagnation points are moved downwards.
2. The effect of circulation is to increase the velocity over the upper surface at the cylinder and to reduce it on the lower surface.
3. Therefore from Bernoulli's equation it follows that the pressure is reduced on the upper surface and increase on the lower surface as result a force is produced a vertically upward called as lift.
4. The streamline pattern is still symmetrical about the vertical axis which follows that still there is no drag.

D'Alembert's paradox:

1. The circulation theory of lift illustrated that for a stationary cylinder neither lift nor drag is produced in the cylinder.
2. And for rotating cylinder lift is produced but still no drag is produced on the cylinder.
3. This is true only under the assumption of ideal fluid flow, but in nature no fluid is ideal. Thus the reality shows, when the real fluid passes over the cylinder lift may or may not be produced but drag is always created.

These discrepancy in the theory and reality is known as D'Alembert's paradox. [13]

2.2 BOUNDARY LAYER

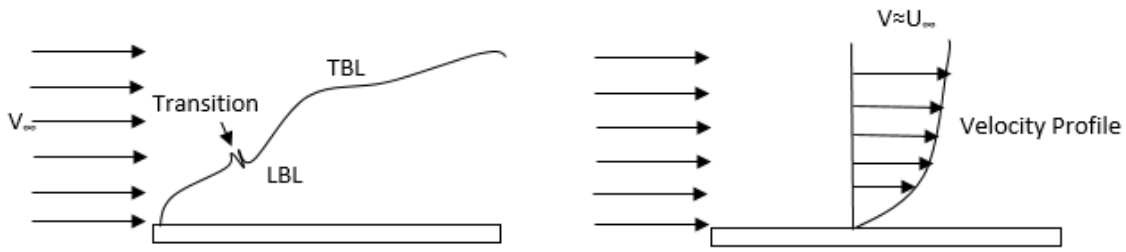

Fig. 2.3 Transition of flow over a flat plate

Definiton

It is a very thin layer of the fluid in the immediate neighborhood of the solid boundary where the variation of velocity from zero at the solid surface to a finite value (0.999 V_∞) in the direction normal to the boundary takes place.

The primary effects of friction are confined to the region closed to the surface called boundary layer. Boundary layer is a shear layer.

The way in which the velocity within the boundary layer varies is shown by means of a velocity profile. As the fluid moves downstream the thickness of boundary layer increases.

Boundary layer thickness:

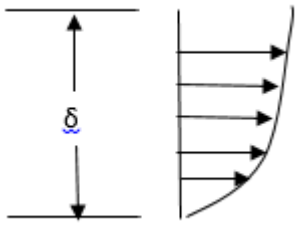

Fig. 2.4 Boundary layer thickness

It is the maximum height up to which the free stream gets affected due to the existence of boundary layer.

Transition:

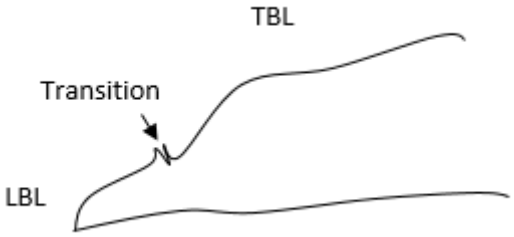

Fig. 2.5 Transition from Laminar to Turbulent

It is the region in the flow field where the transformation of laminar boundary layer. since this region is very small it is commonly referred as transition point.

Factors responsible for transition:

1. **Adverse pressure gradient** (i.e. pressure increasing in the direction of the flow)
   Adverse pressure gradient increases the pressure energy of the fluid and makes the flow turbulent in the nature hence treated as one of the important factor responsible for transition.
2. **Surface roughness or waviness.**
   If the surface is not very smooth and it exhibits some wavy type of surface, it leads to the transition of the flow from laminar boundary layer to turbulent boundary layer.
3. **Free stream turbulence:**
   If the free stream itself is turbulent in nature, it increases the turbulence over rest of the body and hence a favorable condition for the transition.
4. **Heat transfer from surface to the flow:**
   If the body has high temperature than the fluid, the fluid particle experiences higher molecular activities of the fluid particle and makes the flow turbulent.

Separation:

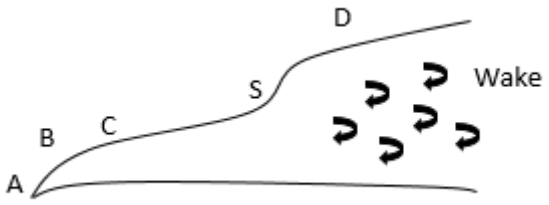

Fig. 2.6 Separation curve

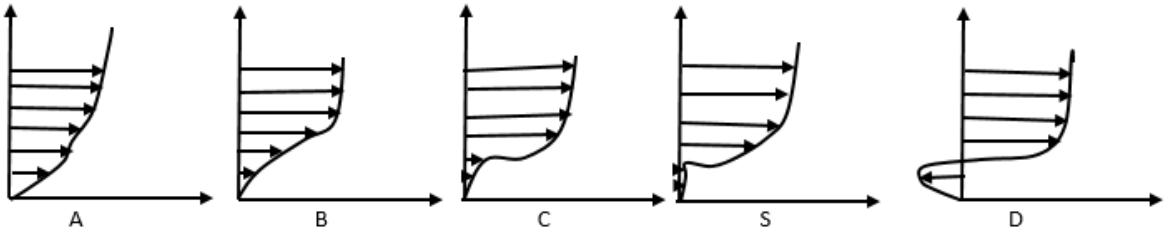

Fig. 2.7 Stages of Separation

1. When the flow passes over the body, the lowest layer of the flow has to spend its kinetic energy to overcome the resistance provided by the body.
2. When the flow starts over the body the closest layer to the solid surface has sufficient Kinetic energy to overcome the resistance as seen in the velocity profile (A)
3. Further as it moves downstream its kinetic energy decreases continuously as the shown in the velocity profile (B) and (C).
4. A condition will be reached where this resistance as shown in the velocity (S). At this point the stream lines will be lifted or thrown away from the solid surface due to lack of the energy and this phenomenon is shown as separation.
5. Beyond the separation point a negative velocity is observed resulting in a region of randomly moving eddying flow known as wake region or dead air region.

Effects of separation:

1. The breakdown of streamline pattern.
2. A violent unsteadiness in the flow.
3. The large and sudden increase in the form drag due to the drastic change in the effective shape of the body.
4. Sudden reduction in the lift of an airfoil.

Table 1 Difference between Laminar and Turbulent Boundary Layer

Sr.no.	**Laminar Boundary Layer (LBL)**	Sr.no.	**Turbulent Boundary Layer (TBL)**
1.	Flow is regular and smooth	1.	Flow is irregular and in random motion
2.	Viscous force is low	2.	Viscous force is low
3.	Inertia force is low	3.	Inertia force is high
4.	Reynolds no. is low	4.	Reynolds no. is high
5.	Kinetic energy is low	5.	Kinetic energy is high
6.	Flow separates easily	6.	Higher tendency to delay the separation

It is expected that the turbulent boundary layer less likely to separate than the laminar boundary layer

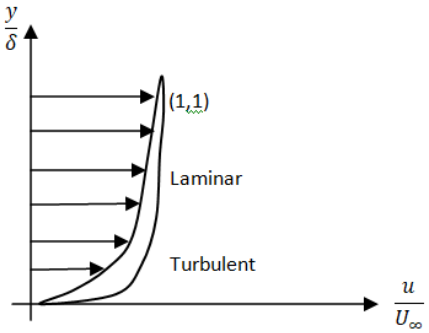

Fig. 2.8 Transition and Separation

1. In a laminar zone the particles in the region closer to the solid boundary layer moves at much slower speed.
2. The particles in the region closer to the solid boundary have to spend their kinetic energy to overcome the resistance offered by the body.
3. The laminar boundary layer has less kinetic energy due to which the velocity of particles near the solid surface falls to zero and hence the chances of separation are reached early.
4. In case of turbulent boundary layer the particles have higher kinetic energy associated with higher molecular activities.
5. Therefore the turbulent boundary layer offers greater resistance to the separation and the flow sticks to the surface for longer duration.
6. The delayed separation results in smaller wake region and therefore lesser drag as shown in Fig. 2.8
7. Hence Turbulent boundary layer will be less likely to separate than Laminar boundary layer
   e.g. providing a trip wire ring on a sphere causes early transition and delayed separation.

A trip wire ring is provided on the sphere to assist the flow:

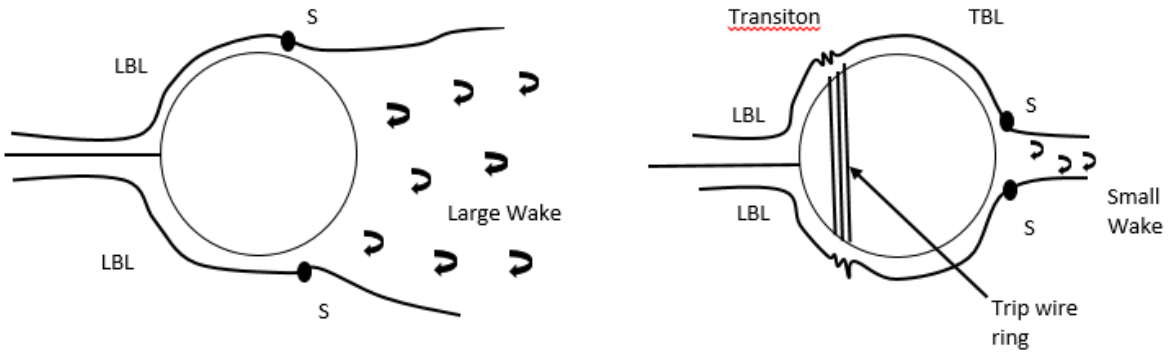

Fig. (a) Fig. (b)

Fig. 2.9 A trip wire is winded on the sphere to assist the flow

1. In laminar zone in plane surface they produced laminar boundary layer around itself. Laminar boundary layer particles in the region closer to the solid boundary layer moves at much slower speed.
2. The particles in the region closer to the solid boundary have to spend kinetic energy to overcome the resistance offered by the body.
3. In Laminar boundary layer there is early separation, more wake region and more drag.
4. If we provide trip wire ring on the sphere turbulent boundary layer from around the sphere.
5. In case of the turbulent boundary layer the particles have higher kinetic energy associated with higher molecular activities.
6. Therefore turbulent boundary layer offers the greater resistance to the separation and flow sticks to the surface for longer duration.
7. The delayed separation results in smaller wake region and therefore lesser drag as shown in fig.(b)
8. Therefore a trip wire is provided to on the sphere to assist the flow.

Seam is provided on the cricket ball:

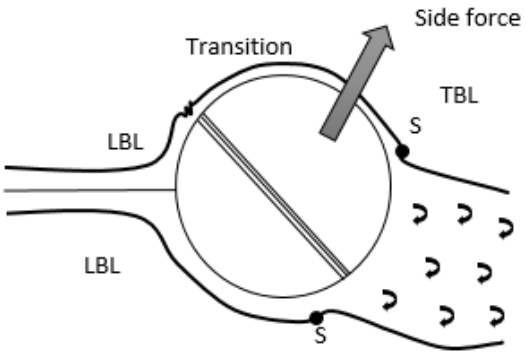

Fig. 2.10 Flow over a cricket ball

1. Consider the ball with its seam at an angle to the flow direction as shown in Fig. 2.10
2. The boundary layer on the lower side of the ball is laminar and therefore early separation occurs on this side of the ball.
3. On the other side the roughness of the seam causes early transition due to which laminar boundary layer is converted into turbulent boundary layer and separation delayed.
4. The results of this symmetry in the streamline pattern is a side force which produces a sidewise movement of the ball as shown in Fig. 2.10
5. Hence the seam is provided on the cricket ball to help the bowler to swing the ball according to his wish.

Dimples are provided on the golf ball.

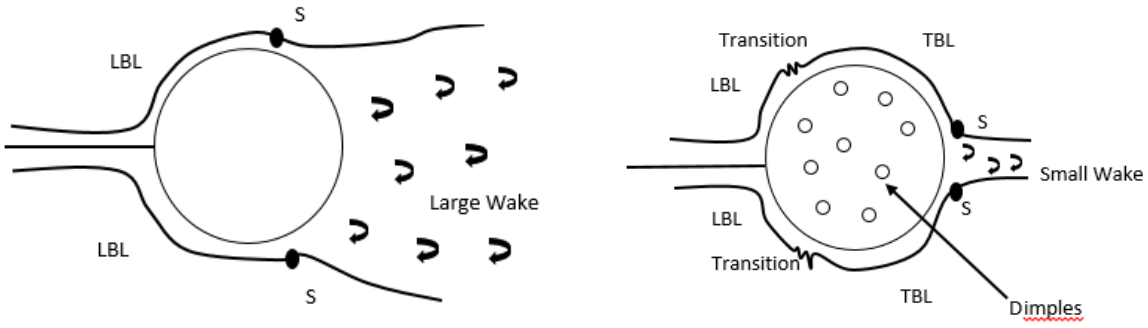

Fig. (a) Fig. (b)

Fig. 2.11 Flow past a surface of golf ball

1. In early days the gold balls were designed with smooth and shiny surface without dimples.
2. The boundary layer pattern over this type of ball is shown in fig (a) where the laminar suffers early separation resulting in large wake region and therefore more drag.
3. And therefore the ball never travelled the expected distance even for the heaviest stroke.
4. Then it was noticed that the older balls travels longer distance than the new balls for the same strength of the stroke.
5. The reason behind this thing is the rough surface of the ball which causes early transition therefore delayed separation, small wake region and hence less drag as shown in fig(b).

6. There after the golf balls were designed with rough surface i.e. with dimples for which the streamline pattern is shown in fig(b).
7. This type of balls used to travel a larger distance even for a lighter strike due to the less drag acting on them.

Turbulent boundary layer is preferred over the outer walls of the Qutub minar

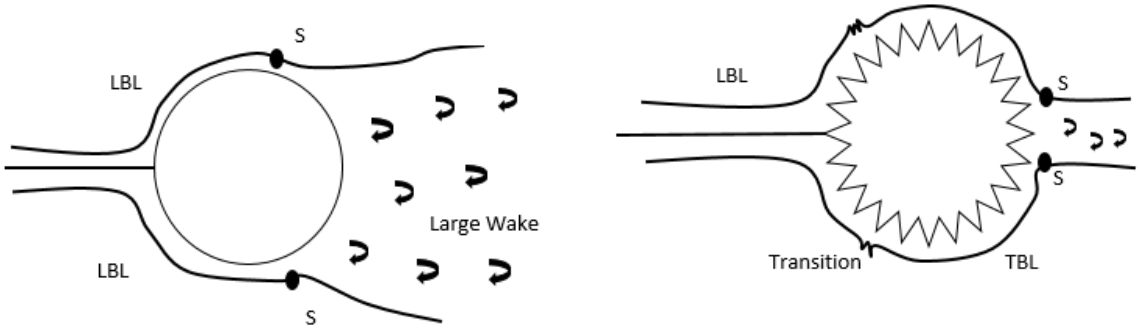

Fig. (a) Fig. (b)

Fig. 2.12 Flow past the wall surface of Qutub minar i.e., Top view

1. The boundary layer pattern for the plane surface as shown in fig(a). If we preferred laminar boundary layer pattern over the outer walls of Qutub minar it creates laminar boundary layer around the minar resulting in early separation, large wake region, more drag and therefore large bending moment about the base of the tower.
2. To withstand with this large bending moment the size of the base is very large which can be practically impossible or economical unacceptable.
3. If turbulent boundary layer is preferred over the outer walls of the Qutub minar, In case of turbulent boundary layer particles have higher kinetic energy associated with molecular activity.
4. Therefore turbulent boundary layer offer the greater resistance to the separation and flow sticks to the surface for longer duration.
5. Turbulent boundary layer causes the early transition, delayed separation small wake region, therefore small bending moment about the base of the Qutub minar.
6. The design for the withstanding this bending moment is simple and economically acceptable.
7. Therefore turbulent boundary layer is preferred over the outer walls of the Qutub minar. [13]

3 PARTICLE IMAGE VELOCITMETRY

Particle Image Velocimetry (PIV) is a non-intrusive optical measurement technique the enables the mapping of instantaneous velocity distributions within planar cross-sections of the flow field. This powerful approach to flow measurement has undergone tremendous development since it was first recognized as a separate method in the early 1980s [14]. Important parameters that should be observed and optimized in each of the individual steps of the PIV technique are described and a set of experimental design rules are given. The factors that determine the measurement uncertainty and limit the attainable dynamic ranges of velocity and spatial resolution are also discussed. Finally, the subject of post-processing PIV data in order to infer the out-of-plane vorticity part and turbulence statistics is briefly discussed.

3.1 INTRODUCTION

The fast advancement of PIV within the last decade has depended on parallel improvements in optics, pulsed lasers, computers and digital recording and image analysis methods. Initially dependent on photographic chronicles, the transcendent variant of the technique today is digital particle image velocimetry (DPIV) which was introduced in the early 1990s by Willert an Gharib [15] and Westerweel [16]. In DPIV, images are acquired digitally and analyzed computationally eliminating all photographic or opto-mechanical processing steps. This has lead to a speed-up of processing times of about two orders of magnitude and made it feasible to study flow statistics with this quantitative visualization technique. Moreover, the appearance of integrated commercial PIV systems has spread the measurement technique from academic fluid dynamics laboratories to industry. Grant [17] provides a general overview of the improvement stages and various perturbations of the PIV technique and also the wide spectrum of applications that PIV is used for today can be described, ranging from geometrically simple flow configurations for the study of turbulence to profoundly specific engineering applications.

3.1.1 PRINCIPLE

The fundamental rule of PIV is very basic and comprises of four general strides as appeared in figure. The flow field is seeded with small tracer particles (seeding) and illuminated by a plane light sheet. The sheet is pulsed at two very closely spaced instants in time and the light

scattered from the particles is recorded either on a single photographic negative or, in DPIV, on two separate frames on a digital sCMOS camera, placed at right angles to the light sheet. The data processing stage subdivides the recorded image into small interrogation areas and subsequently used to determine the average particle image displacement $\Delta \sim X$ in each region. This knowledge and distance of the time interval Δt between the two pulses and the magnification M between the illumination and recording planes then allows the calculation of the instantaneous velocity field, $\sim u = \Delta \sim X/M\Delta t$ [18].

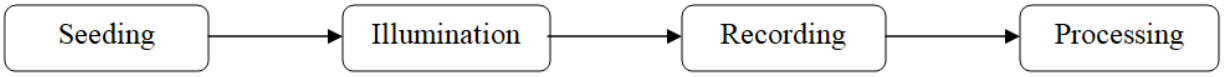

Fig. 3.1 The four general steps of the PIV technique.

3.2 PLANAR PIV SYSTEM

3.2.1 COMPONENTS FOR MOUNTING AND POSITIONING

3.2.1.1 LaVision ultrasonic nebulizer

- Mounted in a water filled reservoir
- Attached to a subwoofer with a tube

3.2.1.2 Imager sCMOS LaVision camera

- 2560 x 2160 pixel resolution (16.6 mm x 14.0 mm sensor size)
- 16 bit dynamic range
- 6.5 μm x 6.5 μm pixel size
- 120 ns minimum interframing time = minimum dt
- 50 Hz (25 Hz double frame mode)

3.2.1.3 Quantel Evergreen 200-15 PIV Laser

- Dual head Nd: YAG laser
- 200 mJ – 15 Hz / cavity

3.2.1.4 Additional optical components

- LaVision light sheet optics with f=-20mm cylindrical lens and adjustable sheet focus distance 100 mm f/2.8 lens with 532/10 nm band pass filter
- Calibration target – 10 cm dual plane, dual sided beam dump

3.2.1.5 Data acquisition and procession units

- Dual quad-core 64 bit Windows7 PC
- LaVision internal Programmable Timing Unit (PTU)
- Up to 16 channel output
- 10 ns resolution
- DaVis FlowMaster software version 10.0.4

3.3 PIV SET-UP

A brief description of the PIV system components associated with each of the four steps shown in figure 1. The accentuation is on giving commonly appropriate rules to legitimate setup of a PIV experiment. The discourse will concentrate on cross-correlation DPIV, in spite of the fact that the more broad abbreviation PIV will be kept up. For an exhaustive depiction of the individual system components, including a discussion of photographic PIV, the reader is alluded to the ongoing book on PIV by Raffel et al. [19] and references in that.

3.3.1 SEEDING

As the seeding particles suspended in the fluid play the job as the genuine speed tests, they ought to in reality be viewed as a major aspect of the instrumentation equipment. It has just been noticed that a uniform and sufficiently high concentration of flow seeding is an essential for an PIV experiment, and another similarly imperative necessity is to maintain a strategic distance from slip between the particles and flow field of intrigue. The seeding particles ought to along these lines, in a perfect world, be impartially light and as little as could be expected under the circumstances, yet sufficiently vas to disperse sufficient light. A trade off between diminishing the particle size to improve flow following and expanding the particle size to improve flow following and expanding the particle size to improve light dispersing is thus necessary. In the present work, notwithstanding, the following qualities of the particles are of more noteworthy concern and this subject is along these lines considered beneath.

Tracking characteristics

The specification of limits on the diameter d_p and density ρ_p of seeding particles is generally founded on their capacity to pursue spatial and temporal gradients in the flow. This might be quantified as far as the slip velocity which is instantaneous velocity $\Delta u = u_p - u_f$ of the

particle (index p) relative to the fluid (index f), and the cut-off frequency f_c which is a measure of the fastest turbulent fluctuations that the particles can follow within a specific precision. To gauge how the physical properties of the seeding particles influence these two parameters, Eq. 3.1 is frequently utilized as a beginning stage. It depicts the unsteady motion of a spherical particle suspended in a turbulent fluid and was derived by Basset in 1888 (see additionally for example Melling [20]):

$$\underbrace{\frac{\pi d_p^3}{6}\rho_p\frac{du_p}{dt} = -3\pi\rho_f \nu d_p \Delta u}_{Stokes' \; drag \; law} + \frac{\pi d_p^3}{6}\rho_p\frac{du_p}{dt} - \frac{1}{2}\frac{\pi d_p^3}{6}\rho_p\frac{d(\Delta u)}{dt} - \text{Fhist} \qquad \textbf{3.1}$$

Where ν and ρ_f are the kinematic viscosity and density of the fluid, respectively, and body forces have been neglected. The first two terms of Eq. 3.1 are the acceleration force and viscous resistance, respectively, equivalent to Stokes' drag law. The third term is the pressure gradient force and the fourth term is known as the added mass and represents the fluid resistance to the accelerating sphere. The final term, F_{hist}, is the so-called Basset history integral which defines the resistance caused by the unsteadiness of the flow field [20].

A broad discussion of Eq. 3.1 and its solution for turbulent flow under various conditions has been given by Mei [21]. Solutions may be example expressed in terms of the relative amplitude and phase response of the instantaneous fluid and particle motions [22] or as the proportion of the fluctuating energies of the time-averaged motions [23]. Subjectively, the solutions are directed by the density ratio $R = \rho_p/\rho_f$ between the particle and fluid which, in turn, relies upon whether the analysis is performed in a gas or a fluid.

Large density ratios:

For fluid or solid particles suspended in gases, corresponding to PIV experiments in air, R is normally of the order 103 and Eq. 3.1 diminishes to Stokes' drag law which is the condition of particle motion in the limit of creeping flow. For this situation the velocity slip might be evaluated from

$$\Delta u = -\frac{d_p^2 R}{18\nu}\frac{du_p}{dt} = \tau_p\frac{du_p}{dt} \qquad \textbf{3.2}$$

Given the acceleration du_p/dt is known. The relaxation time $\tau_p = -(d_p^2\, R)/18\nu$ is a measure of the characteristic response time of the particles to velocity changes in the fluid which are

regularly expected exponentially [19]. The proportion among τ_p and a characteristic time scale τ_f for the turbulence in the fluid, e.g. the Kolmogorov time scale, defines the Stokes' number

S = τ_p/τ_f

So as to estimate the cut-off frequency f_c of seeding particles, Mei [21] considered the unsteady drag on a stationary sphere encountering a high-frequency oscillation of the fluid flow $u(t) = \tilde{u}(\omega)e^{-i\omega t}$ in which $\tilde{u}(\omega)$ is the amplitude of the velocity fluctuation with angular frequency ω. Mei [21] then demonstrated that the energy transfer function is given by

$$|H(\omega)|^2 = |H(S_\varepsilon)|^2 = \frac{(1+S_\varepsilon)^2 + (S_\varepsilon + \frac{2}{3}S_\varepsilon^2)^2}{(1+S_\varepsilon)^2 + [S_\varepsilon + \frac{2}{3}S_\varepsilon^2 + \frac{4}{9}(R-1)S_\varepsilon^2]^2} \qquad \textbf{3.3}$$

Where H(ω) is the frequency response function of the particle and $S_\varepsilon = d_p\sqrt{\omega/8\nu}$ is a Stokes number. Defining cut-off frequencies of the particle based on either 50% or 200% energy response, $S_{\varepsilon,c} = \{S_\varepsilon : |H(S_\varepsilon)|^2 = \frac{1}{2} or\ 2\}$, the cut-off Stokes' number $S_{\varepsilon,c}$ can be obtained from Eq. 3.3 as a function as a function of the density ratio R. For this reason Mei [21] gave the accompanying interpolation formula:

$$S_{\varepsilon,c} \approx \left[\left(\frac{3}{2R^{1/2}}\right)^{1.05} + \left(\frac{0.932}{R-1.621}\right)^{1.05}\right]^{1/1.05} \quad \text{for R} > 1.621 \qquad \textbf{3.4}$$

This, finally, permits the cut-off frequency of the particle to be evaluated from

$$f_c = \frac{\nu}{\pi}\left(\frac{2S_{\varepsilon,c}}{d_p}\right)^2 \qquad \textbf{3.5}$$

Eq. 3.5 will be utilized to estimate f_c for the particles utilized in the PIV estimations of the air flow past a square cylinder. A review by Melling [20] of a scope of seeding materials demonstrated that a width or diameter of 2-3 μm is commonly satisfactory for a frequency response of 1 kHz, necessitating that the particle pursue the fluid movement inside 1%. A superior frequency response up to 10 kHz for the most part requires particle distances or diameter across not surpassing 1 μm.

Small density ratios:

For small particles with a density near to that of the fluid, which is the run of the mill circumstance experienced when performing PIV estimations in water, Eq. 3.1 is more difficult to unravel. Moreover, body powers which were unequivocally dismissed in Eq. 3.1 might be of significance. Subsequently, Agüí and Jiméney [24] on the other hand connected the idea of the energy transfer function and found that the following mistake of the speed might be evaluated from

$$\frac{|\Delta u|^2}{|u_f|^2} \approx 0.018 \frac{(R-1)^2}{S_0^2} \qquad \textbf{3.6}$$

Where S_0 is a Stokes number defined as $S_0 = d_p\sqrt{\nu/\omega_0}$ and $\omega_0 = 2\pi f_0$ is the angular frequency of the turbulence fluctuations associated with the typical eddy frequency f_0. This gives the accompanying appraisal of the slip velocity for small density ratios [25]:

$$\left(\frac{\Delta u}{u_f}\right)^2 \approx \left(\frac{\rho_p - \rho_f}{\rho_f}\right)^2 \frac{d_p^2 f_0}{9\nu} \qquad \textbf{3.7}$$

Eq. 3.7 will be utilized in area 6.4.2 to appraise the slip velocity associated with the seeding particles used in the centrifugal impeller measurements.

3.3.2 ILLUMINATION AND RECORDING

A pulsed double-cavity Nd:YAG laser is commonly required in PIV to give sufficient illumination energy in short duration pulses to record unblurred pictures of the particles in the flow. The pulsing laser beams are controlled into a two-dimensional light-sheet by cylindrical and spherical lenses, see for example Stanislas and Monnier [26] for practical guidelines on the optical setup.

In the predominant PIV variation today, cross-relationship DPIV, the light scattered from the illuminated particles is recorded on advance cameras with light-delicate CMOS sensors that example the light intensity over little regions alluded to as pixels. These cross correlation cameras store the two exposures on separate frames and thereby eliminate the directional ambiguity associated with double exposed images. Present digital cameras normally contain sCMOS arrays with 10242 to 20482 pixels. This resolution is still moderate compared to photographic PIV but high-resolution sCMOS cameras are probably going to wind up accessible sooner rather than later. Regarding temporal resolution, the greatest feasible redundancy rate of both Nd:YAG lasers and cross correlation sCMOS cameras is in the order

of 10-30 Hz which is much slower than the time sizes of generally flows. Hence, despite the fact that PIV is an instantaneous technique, genuine time-resolved recordings of quick flows, for example, those investigated in this work are still not feasible.

An essential parameter influencing the exactness of PIV is the measure of the recorded particle images in the recording plane. This depends on the particle diameter dp as well as on the point reaction function of the camera lens. On account of diffraction limited imaging, the point reaction function is an Airy function and the image of a finite-diameter particle will shape a diffraction design with diameter (see for example [27])

$$d_s = 2.44(M+1)f^{\#}\lambda \qquad \textbf{3.8}$$

Where $f^{\#} = f/D_a$ is the numerical aperture (f-number) of the camera lens, defined as the proportional between its focal length f and aperture diameter D_a, and λ is the laser light wavelength. Ignoring focal point distortions, a gauge of the all out particle image diameter d_t is given by [27]

$$d_t = \sqrt{M^2 d_p^2 + d_s^2} \qquad \textbf{3.9}$$

It is seen that for small magnifications M which emerge when estimating huge zones in the flow, the particle image size is predominantly administered by the diffraction-limited spot, dt ≈ ds. Moreover, so as to get a sharp image the particle needs to fall inside the focal length δz of the camera lens which might be assessed from [28]

$$\delta z = 4\left(1+\frac{1}{M}\right)^2 f^{\#2}\lambda \qquad \textbf{3.10}$$

Raising the numerical aperture $f^{\#}$ prompts an expansion of both the particle image diameter and the focal depth, yet thusly causes a decrease of the light intensity falling on the sCMOS. The above infers that PIV estimations require a cautious optimization of the parameters dp, M and $f^{\#}$.

3.3.3 IMAGE PROCESSING

So as to remove the dislodging data from PIV images, a factual technique is connected. This comprises of deciding the average linear displacement in each every interrogation area IA utilizing cross correlation techniques. The discrete spatial cross-correlation Φ as for two images is given as [19]

$$\Phi(k,l) = \sum_{i=1}^{D_I} \sum_{j=1}^{D_I} I_1(i,j) I_2(i+k, j+l) \qquad \textbf{3.11}$$

Where I_1 and I_2 are the light intensities, for example 2D gray scale values, removed from the two images and D_I is the pixel width of the square interrogation area. By applying Eq. 3.11 for different shifts (k,l), a correlation plane is framed which factually measures the level of match between the particle images in the two interrogation areas. The pinnacle position in this correlation plane at the point estimates the particle displacement.

Computationally, the twofold summation in Eq. 3.11 is costly and is more effectively performed in the frequency domain. Favorable position is in this manner taken of the correlation theorem which expresses that the cross-correlation of two functions is proportional to a mind boggling conjugate augmentation of their Fourier transforms changes $\mathcal{F}$ [19]

$$\Phi(k,l) = \mathcal{F}^{-1}[\mathcal{F}(I_1)\mathcal{F}^*(I_2)] \qquad \textbf{3.12}$$

Where $\mathcal{F}^{-1}$ denotes an inverse Fourier transform and * a complex conjugate. Executing Eq.(2.13) utilizing FFT algorithms diminishes the number of operations to O ($N^2 \log_2 N$) compared to O (N^4) activities in the spatial space. Figure 2.2 demonstrates the general strides of the FFT based velocity vector assessment system. For subtleties on the hypothesis and usage of DPIV, the reader is alluded to Willert and Gharib [15] and Westerweel [16].

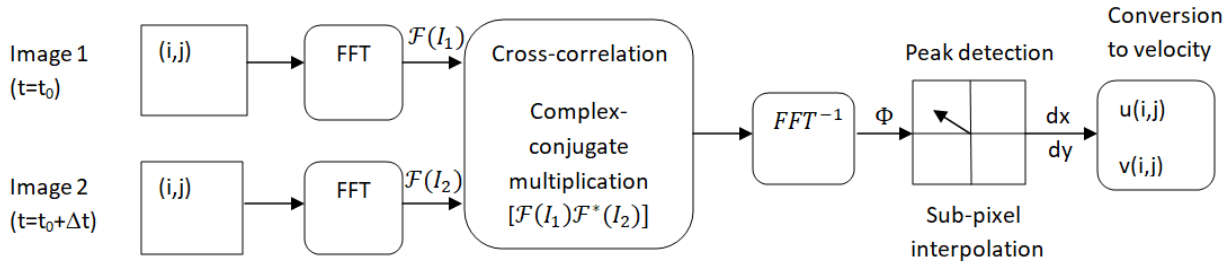

Fig. 3.2 PIV cross-correlation velocity evaluation velocity implemented using Fast Fourier Transforms Willert and Gharib [15]**).**

As the correlation function exists for whole number shifts, the maximum correlation value just allows the displacement to be resolved with an uncertainty of ± 0.5 pixel. To expand the exactness, sub-pixel interpolation schemes are connected which normally estimate the pinnacle area to within ± 0.1 pixel. Usually utilized interpolation schemes are the Centroid estimator and the Parabolic and Gaussian peak fits, which are all 3-point estimators. The

Gaussian estimator for the most part gives a superior approximation of the actual peak shape and is along these lines habitually utilized. A few creators have examined the effect of peak-finding schemes on the velocity information, see for example [16], [29]. Following the vector evaluation procedure, usually to apply a type of approval rule so as to distinguish and expel false vectors that outcome from poor correlations due to insufficient seeding density or low signal-to-noise proportion SNR. An ordinarily applied identification criteria is the median displacement scheme by Westerweel [16], yet an assortment of elective techniques to identify these alleged exceptions and potentially supplant them with vectors interpolated from the encompassing information have been created, see for example [30].

3.4 UNCERTAINTY QUANTIFICATION

3.4.1 INTRODUCTION

The essential test to any PIV processing scheme is to choose the ideal spatial resolution-mainly determined by interrogation window size and overlap factor for a given picture/image quality and signalto-noise ratio or information density ratio. In many cases, this is not uniform across the image or varying from image to image. Ordinarily, one endeavors to discover some compromise in interrogation window size and other handling parameters which work sensibly well all over. Rather, it is favorable to locally adjust the spatial resolution.

For this reason, a few adaptive PIV techniques have been formed thinking about local seeding densities, flow gradients, or physical constraints like walls, locally adjusting the interrogation window position, size, and shape ([31] [32] [33]). These techniques have shown to reduce the systematic and random noise level significantly, specifically near object surfaces.

3.4.2 METHODS

The denoising scheme described here is limited to planar velocity fields with u, v and perhaps w components together with uncertainty values Uu, Uv, Uw, on a 1-sigma level, i.e., the genuine velocity value utrue is relied upon to exist in u $\pm$ Uu with a likelihood of 68%. Denoising is done autonomously for each vector of the flow field.

Toward the start, for every vector component (u, v and w) , a second-order 2D-polynomial function is fitted to a 5 x 5 vector neighborhood around the center vector. The uncertainty of the vectors in the 5 x 5 neighborhood is arrived at the midpoint of and taken as a kind perspective in the accompanying. Vectors simply outside the center 5 x 5 region (white squares in Fig. 3.3) are tested if they ought to be added to the filter kernel. Vector a and, in the meantime, vector d on the contrary will be included if both contiguous internal vectors b and c are a piece of the filter kernel, and if all segments (u, v, w) of vectors a and d are within an uncertainty band around the fitted polynomial function, as appeared in Fig. 3.4.

The uncertainty band Fig. 3.3 is given by $\pm$S times the uncertainty (given on a 1-sigma level), where S is a under-selected filter strength, as demonstrated later regularly set to around 2.5 – 3.5.

A limited band of $\pm$1-sigma would be excessively tight, since with a likelihood of 32%, a vector falls outside this range keeping the development of the filter kernel. The methodology stops when no more vectors are included or when a client chose greatest bit estimate is come to. Toward the end, the frequently very sporadic state of the filter kernel is changed to a closest ellipse (Fig. 3.5). The distinction in execution with and without ellipse fitting is just minor. At that point, LPA is executed on the vector field inside the filter kernel, and the middle vector is supplanted by the estimation of the polynomial function at the inside area. Since the spatial subordinated of the flow field are promptly accessible from fitted polynomial capacity, they are stored, example for ensuing vorticity or divergence computation.

At last, the system processes another uncertainty for every vector segment utilizing the uncertainty propagation rules sketched out in Sciacchitano and Wieneke [34]. A disentangled variant is utilized here by taking the reference uncertainty divided by sqrt(N_{eff} – 6), where N_{eff} is the quantity of autonomous vectors in the final filter kernel and 6 is the quantity of parameters (degrees of freedom) of the 2nd order 2D-polynomial function. Generally, N_{eff} is the total number of vectors in the filter kernel isolated by the quantity of vectors within the size of the interrogation window. For instance, with an interrogation window size of 32 x 32 pixel and 75% overlap, there will be 16 vectors inside the window. On the off chance that one would cover up these 16 vectors, there will be viably very little reduction of the uncertainty and noise, since the errors of all vector are firmly correlated.

It is likewise important to refresh the spatial resolution of the vector field, which is identified with the spatial autocorrelation coefficients between neighboring vectors. Because of variable filter size and shape, this is distinctive for every vector in magnitude and direction, like the adaptive PIV techniques with changing interrogation window sizes and shapes. A completely right treatment is confounded and would require the capacity of numerous additional correlation values for every vector for resulting uncertainty propagation. Once more, a streamlined adaptation is embraced here setting the spatial resolution to the average linear dimension of the filter kernel. It should be appeared, if this is adequate for precise uncertainty quantification when the directional dependence of the viable spatial resolution winds up imperative, example for the vorticity field. The proposed denoising plan takes normally a couple of moments of processing time on a standard PC. It can without much of a stretch be reached out to volumetric information and to the time area.

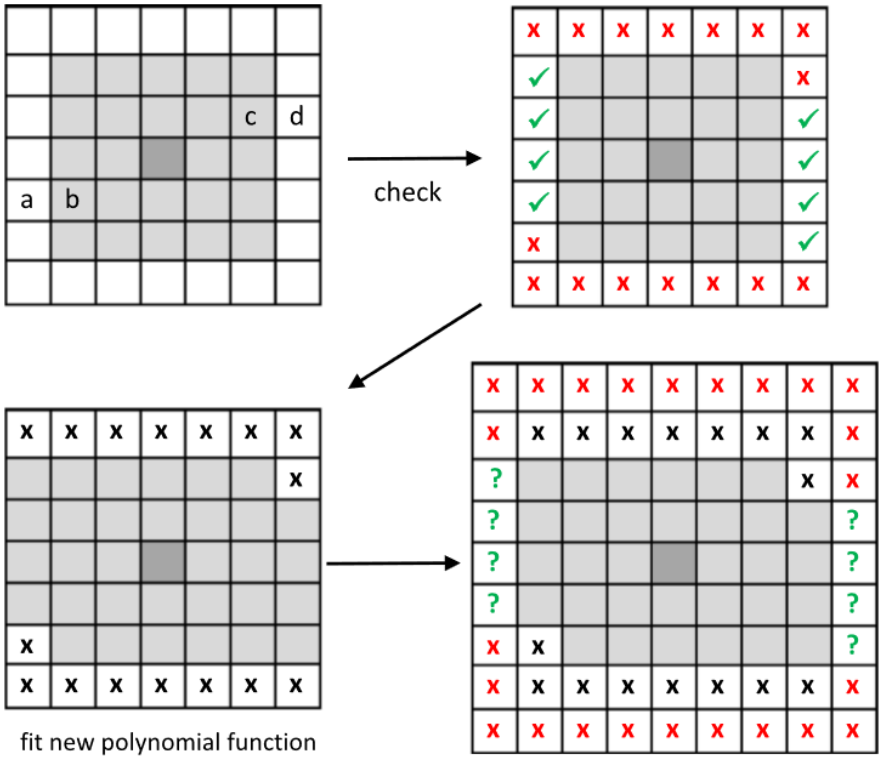

Fig. 3.3 Adding another shell to filter kernel [33]

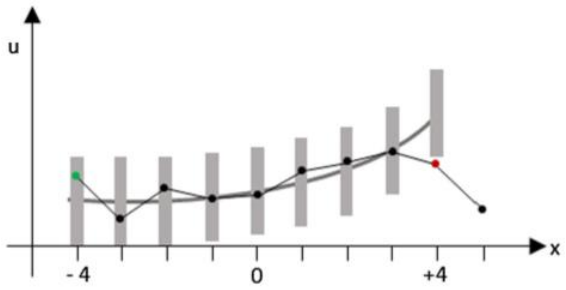

Fig. 3.4 Polynomial function processed around the centre at x = 0 with information somewhere in the range of -3 and +3 and extrapolated to ± 4. Red vector at ± 4 is rejected, since it lies outside the gray uncertainty band. [33]

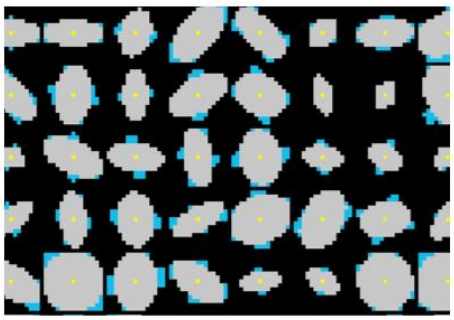

Fig. 3.5 Final filter kernel (blue) is converted at an ellipse (gray) shown for every 13th vector. [33]

3.4.3 SYNTHETIC DATE VALIDATION

The denoising plan is first tried on a synthetic vector field with a wide scope of spatial wavelengths L and signal-to-noise ratios (velocity dynamic range). The vector field contains 200 x 75 vectors with a grid spacing d of 4 pixel. The (genuine) flow field contains vortices of different sizes with spatial wavelengths of 512 pixel on the left and 32 pixel on the privilege of the picture with a consistent (genuine) amplitude of 1 pixel (Fig. 3.6 top). Vortices establish a more testing case than simple shear flows, where the filter kernel shape can be firmly lengthened along the shear.

Any PIV algorithm has a limited spatial resolution proportionate to a characteristic filter length L_{sr} decreasing small scale vacillations. Here, it is expected that L_{sr} is 16 pixel, identical to 4 vectors, which is like utilizing 16 x 16 pixel interrogation windows with 75% overlap. The filter length L_{sr} as the opposite of the spatial resolution is characterized here as the aggregate of the auto-correlation coefficients between the errors of neighboring vectors [34]. In the event that PIV would be a straightforward single-pass linear top-cap filter averaging the displacement data within an interrogation window of L x L pixel, then L_{sr} would be equivalent to L, as can be effectively checked. The vector field is sifted here with a Gaussian filter function

$(\propto \exp(-\frac{x^2}{2\sigma^2}))$ of identical filter length $L_{sr} = \sigma\, sqrt(4\pi)$. This prompts a noteworthy decrease in amplitude for small wavelengths, e.g., about half for $L/L_{sr} = 2$ (Fig. 3.6 middle and bottom). The accurate spatial frequency relies upon subtleties of, e.g., the predictor-

corrector scheme of a multi-pass PIV algorithm. This smoothing is incorporated to put the clamor level and its decrease by the anisotropic denoising scheme in context to the unavoidable amplitude decrease of little wavelengths due to the limited spatial resolution of the PIV algorithm itself.

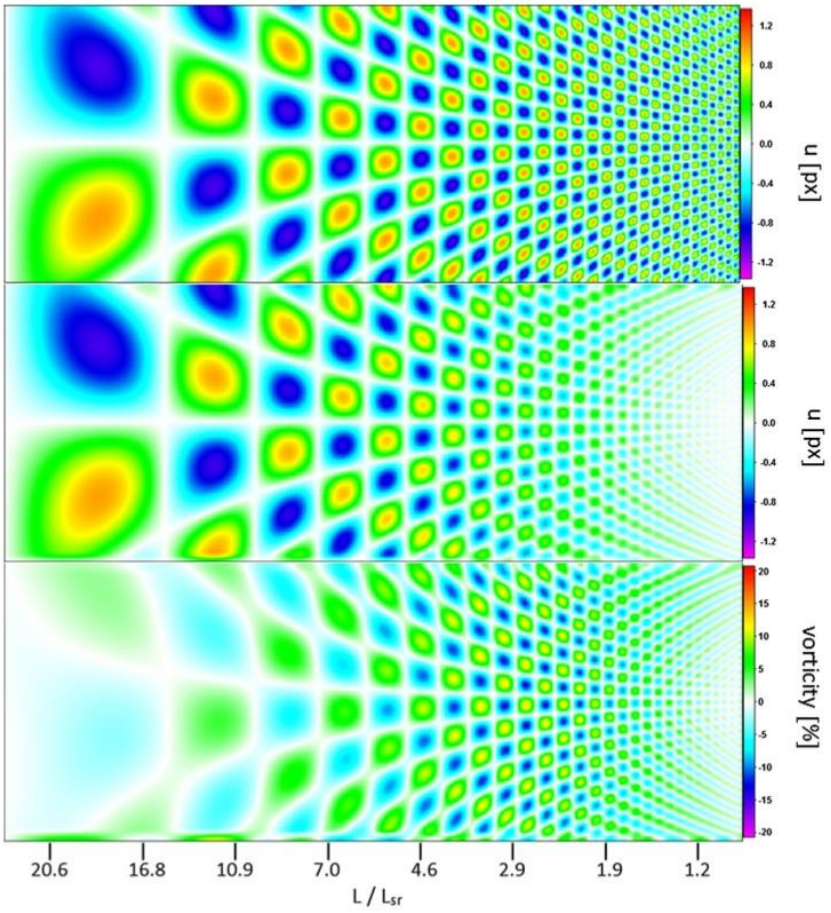

Fig. 3.6 Synthetic vector field with constant fluctuation amplitude (top) and after taking the finite spatial resolution of a PIV algorithm into account showing u component (middle) and vorticity (bottom) [33]

Noise levels of 0-100% are added to every vector part, again subject to the PIV spatial filtering, which prompts privately correlated noise components between neighboring vectors. This ends up essential while applying privately bound averaging, where the noise is almost no decreased, since it is privately corresponded. Seen another way, neighborhood averaging/denoising must be done over a kernel size bigger than L_{sr} to end up viable. The extreme filter kernel size is set to 41 x 41 vectors. Last processed kernel sizes are commonly in the scope of 5-15 vectors toward every path.

Fig. 3.7 demonstrates the u part with expanding noise level from top to bottom of the original vector field and after denoising with strength S of 1, 2, 2.5, 3 and 4 (from left to right). For

zero noise level (top), the denoising scheme does not change the vector field separated of marginally diminishing the spatial resolution, i.e., expanding L_{sr} from 16 to 19, because of the underlying 5 x 5 polynomial relapse, which is constantly done. This is scarcely unmistakable on the topright, where the sufficiently of little scale variances is diminished marginally.

For low noise levels, the technique precisely recuperates the round stat of vortices for practically all wavelengths Vast-scale vortices with bigger kernel sizes are recouped even at 100% noise level. For smaller wavelengths further to one side, the denoising method can decrease the noise as long as the genuine variances are bigger than the mistakes. Past that, the algorithm cannot recognize genuine and loud fluctuations any longer. Here, given a sufficient filter, the vector field is basically averaged over large regions. The algorithm accept that everything is noise (see base right of the noise plot in Fig. 3.8). The ideal filter strength is by all accounts somewhere in the range of 2.5 and 3.0, sufficiently able to dispense with noise over conceivably vast locales for bigger wavelength while not smoothing over true fluctuations.

The execution of the denoising plan is measured in Fig. 3.9 plotting the nearby rms of the noise for a filter strength of S = 3 as an element of wavelength for the distinctive noise levels of 0-100% (0-1 px). For bigger wavelength $L/L_{sr} > 10$, th noise is diminished by a factor of 2, up to a factor of 4 now and again and bigger wavelengths. For substantial noise levels > 50%, just wavelengths $L/L_{sr} > 15$ are recouped, which isn't astounding, since even outwardly it is hard to recognize smaller vortices in the noisy vector field. Smaller wavelengths are essentially covered up as the algorithm is unfit to recognize genuine vortices and noise. In this way, the general noise level is diminished, yet concealed flow structures are additionally evacuated.

For the noise-free vector field, the error increments for small wavelengths (L/L_{sr} = 1-3) by about 5% of the true amplitude because of the 5 x 5 polynomial relapse, which, as referred previously, prompts 15% lower spatial resolution. In any case, one needs to remember that for these wavelengths, the amplitude decrease because of the spatial filtering impact of PIV is at rate above half.

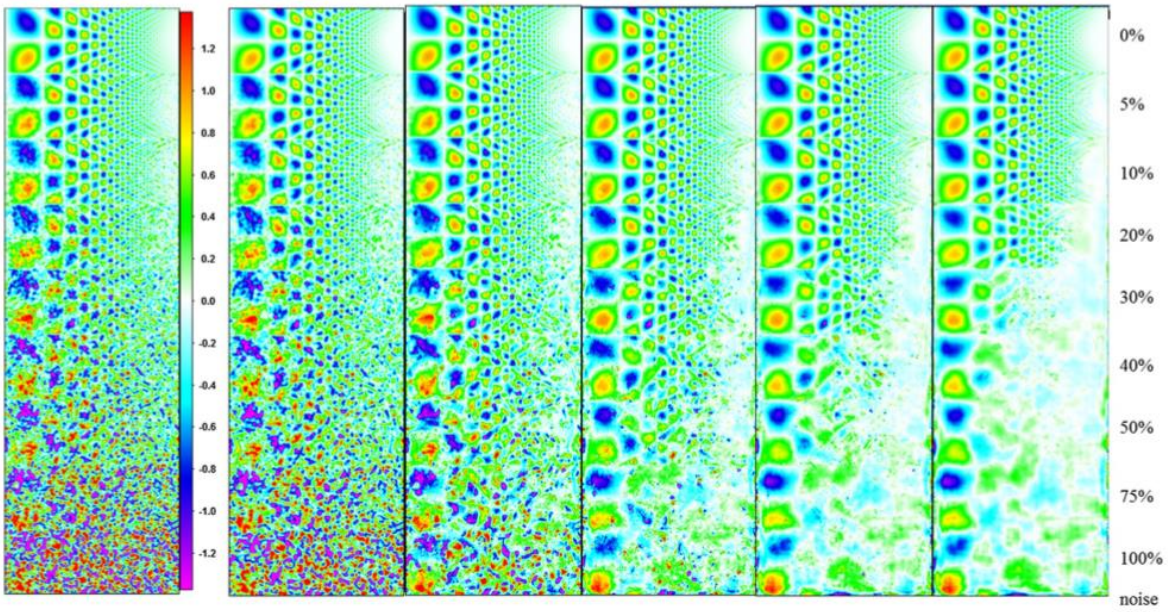

Fig. 3.7 Original vector field and after denoising with strength S = 1, 2, 2.5, 3, and 4 from left to right. Noise level 0-100% from top to bottom. Color = u component [33]

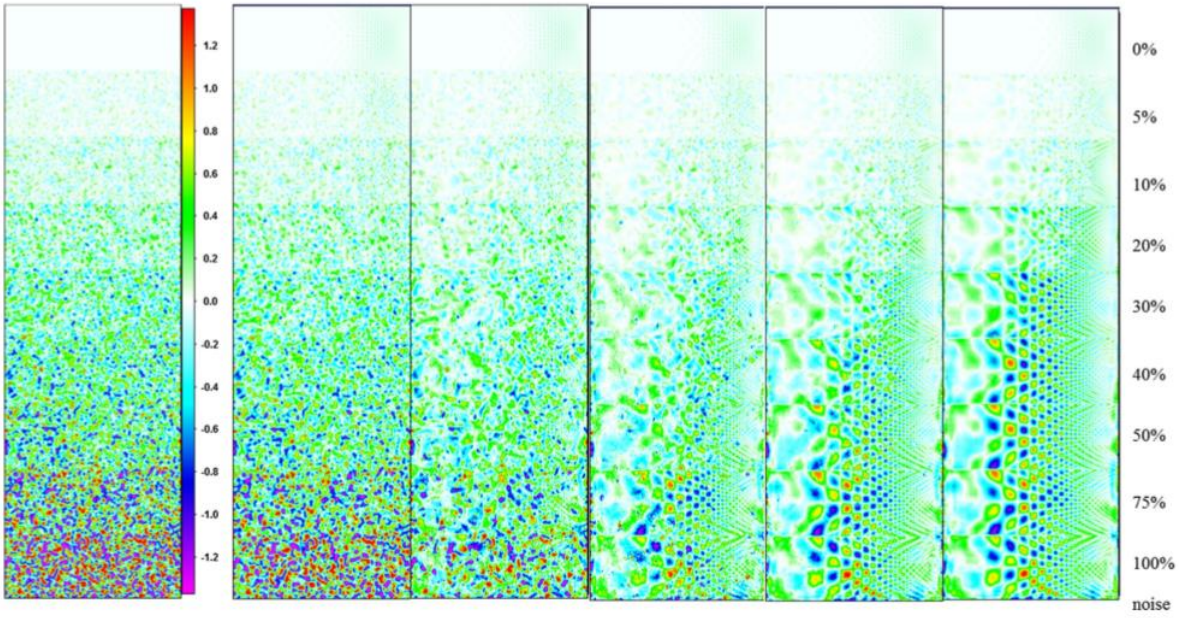

Fig. 3.8 Original noise and after denoising (equal to Fig. 5 minus Fig. 4 middle) with strength S = 1, 2, 2.5, 3, and 4 from left to right. Noise level 0-100% from top to bottom. Color = u component of noise. [33]

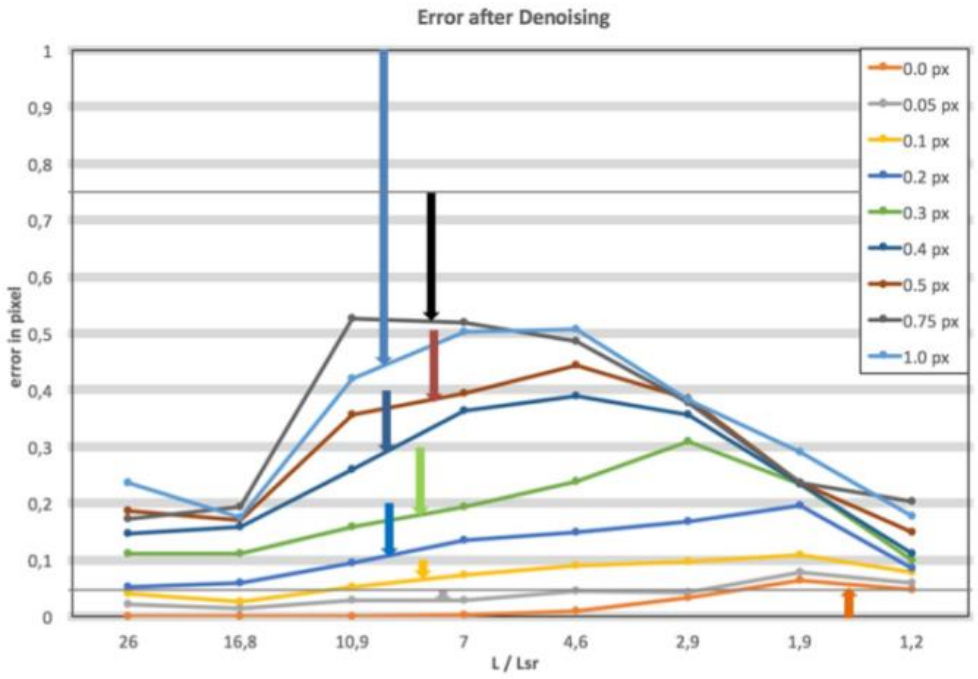

Fig. 3.9 Remaining noise level after denoising as a function of spatial wavelengths for various unique noise levels of 0- 1 px. [33]

The denoising plan has been contrasted with a standard 2nd order request polynomial relapse filter with a fixed kernel size of 5 x 5 to 11 x 11 vectors and a top-cap smoothing filter over 9 x 9 vectors for the case of 20% (0.2 px) noise level (Fig. 3.10). For extensive wavelengths, the polynomial relapse filter diminishes the noise level with progressively bigger filter kernels. The top-cap 9 x 9 filter performs superior to polynomial attack of 11 x 11, since it is generally identical to a polynomial filter of 20 x 20 vectors. For the transitional scope of L/L_{sr} somewhere in the range of 2 and 7, the polynomial relapse filter even builds the noise level, since the decrease of irregular noise is not exactly the additional noise added because of expanded truncation blunders, i.e., smoothing the genuine stream changes. Plainly, the anisotropic denoising noise filter outflanks every single other plan due to locally adjusting the kernel size to the wavelength of the genuine flow fluctuations.

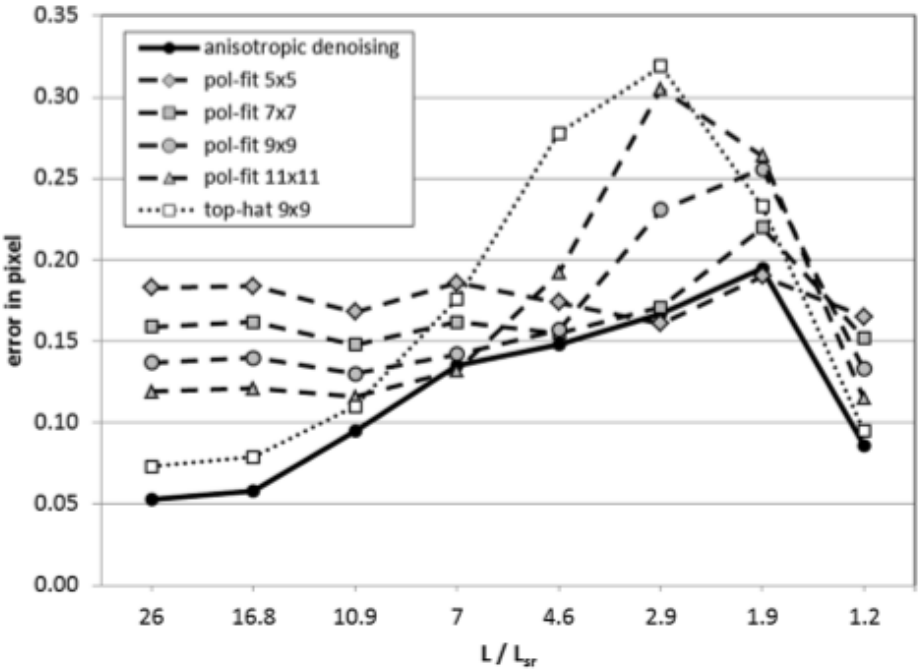

Fig. 3.10 Comparison of anisotropic denoising with the 2nd- order polynomial relapse filter with 5 x 5 to 11 x 11 vector kernel and 9 x 9 top-cap smoothing filter. Original noise level = 0.2 pixel. [33]

4 PLANAR-LASER INDUCED FLUORESCENCE

4.1.1 INTRODUCTION

Planar Laser Induced Fluorescence (PLIF = LIF Imaging) is an exceptionally sensitive laser imaging technique for species concentration, mixture, fraction and temperature measurements in fluid mechanical processes, sprays and combustion systems. LIF imaging is a particle specific visualization method with high spatial and temporal resolution. In the event that the fluid itself contains no LIF-active species (like N_2, CH_4 or water), flow seeding with fluorescent markers (tracers) is utilized for scalar flow field imaging (Tracer-LIF) [35].

The most widely recognized utilization of LIF in fluid flows is two-dimensional planar laser-induced fluorescence (PLIF). The focus of this method is on the quantitative utilization of PLIF to water flows (for PLIF in vaporous flows, see Van Cruyningen et al. 1990). While three-dimensional LIF procedure isn't broadly talked about in this work. In all types of LIF, a laser is utilized to energize fluorescent species within the flow. Normally, the tracer is a natural fluorescent dye, for example fluorescein or rhodamine. The dye retains a part of the excitation energy and precipitously re-produces a part of the absorbed energy as fluorescence. The fluorescence is estimated optically and used to construe the local concentration of the dye.

4.1.2 THEORETICAL BACKGROUND

4.1.2.1 General fluorescence theory

The general connection between local fluorescence F, local excitation intensity I, and local concentration C has the structure

$$F \propto \frac{I}{1 + I/I_{sat}} C \qquad \textbf{4.1}$$

Where I_{sat} is the saturation intensity for the dye. Fluorescence saturation happens when the rate of excitation surpasses the fluorophore deactivation rate [36], prompting the non-linear connection among F and I. Be that as it may, on the off chance that $I \ll I_{sat}$, the excitation is called "weak", and Eq. 4.1 is linearized to the structure

$$F \propto IC \qquad \textbf{4.2}$$

Unless generally noted, weak excitation (and therefore the legitimacy of Eq. 4.2) is accepted throughout this review. As point by point by in Sect. 3.2, high dye concentrations can deliver non-linearity in fluorescence due to absorption-related changes in the local value of I, but Eq. 4.2 gives a basic technique to trial assurance of local concentrations throughout estimation of F. In any case, the local excitation intensity is ordinarily obscure, isn't autonomously estimated, and can change spatially and transiently as indicated by the immediate fixations along the beam way. As per the Beer-Lambert law, absorption causes a ray of light with intensity I passing an infinitesimal distance dr through a solution with dye concentration C to encounter an intensity change

$$\frac{dI}{I} = -\epsilon\, C\, dr \qquad \textbf{4.3}$$

Where ϵ is an absorption (or eradication) coefficient [37]. The local intensity of a ray passing from $r=r_0$ to $r=r_1$ through a spatially variable field is thus

$$I(r_1) = I(r_0) exp\left[-\varepsilon \int_{r_0}^{r_1} C(r) dr\right] \qquad \textbf{4.4}$$

Lessening along a way from r_0 to r_1 is negligible if

$$\epsilon \int_{r_1}^{r_2} C(r) dr \ll 1 \qquad \textbf{4.5}$$

For a uniform fixation field, this imbalance decreases to $\varepsilon bC \ll 1$, where $b = r_1 - r_0$. Frameworks with way lengths and fixations that fulfill Eq. 4.5 are called "optically thin" (Melton and Lipp 2003). A small amount of light energy absorbed locally by the color is in this way radiated as fluorescence in the discharge band. The proportion of light energy radiated to that absorbed is known as the quantum efficiency, ϕ. Consider an infinitesimal right kaleidoscopic volume arranged along the pivot of the incident excitation ray, with a volume dV = dr dA, where dr is the length of the prism in the beam course, and dA is the crosssectional area normal to the beam. A uniform dye concentration C inside the volume enlightened by a neighborhood excitation intensity I fluoresces omnidirectionally with power

$$dF = -\phi\, dI\, dA \qquad \textbf{4.6}$$

Equations 4.3 and 4.6 consolidate to give

$$dF = \phi\, \epsilon I\, C\, dV \tag{4.7}$$

Which is formal proclamation of Eq. 4.2 along a beam way, with I given by Eq. 4.4

4.1.2.2 Theory as applied to PLIF

For most PLIF applications, a spiral laser sheet is formed by a narrow beam passing through sheet optics situated at the root (Fig.). At outspread separations that are huge contrasted with the approaching pillar width, the sheet will have an intensity dissemination of the general form

$$I(r,\theta,z) = P\, a(r,\theta) f(r) g(\theta) h(z) \tag{4.8}$$

Where P is the power in the approaching pillar, and a(r,h) is the dimensionless construction along beam ways due to dye absorption, which, from Eq. 4.4, is

$$a(r,\theta) = exp\left[-\epsilon \int_0^r C(r',\theta) dr'\right] \tag{4.9}$$

The unattenuated spatial intensity conveyance of the sheet is f(r)g(h)h(z). For the spiral sheet appeared in Fig. , f(r) = r-1. The functions g(h) and h(z) rely upon the state of the first pillar and idea of the sheet-shaping optics, and are defined such as an extent that they each incorporate to solidarity over the whole h and z scopes of the sheet, separately. Regularly, the flow is imaged from a camera placed normal to the laser sheet. Consider a small area DA = rDrDh in the plane of the sheet. The camera will image fluorescence from a privilege kaleidoscopic volume DV.

Framed by anticipating DA over the width of the sheet (i.e., the whole degree of h(z). Integrating Eqs. 4.7 and 4.8 over this volume gives the total fluorescence

$$F = \phi \epsilon P\, a(r,\theta) f(r) g(\theta) C \Delta A \tag{4.10}$$

Where it is comprehended that C is presently the focus arrived at an average of over the little imaged volume DV, with the normal weighed in the z direction by h(z). Accepting that any reabsorption of fluoresced light by color along the receiving path [38] is negligible, the fluorescence intensity imaged at any camera pixel location (i,j) comparing to facilitate (r,h) is in this way

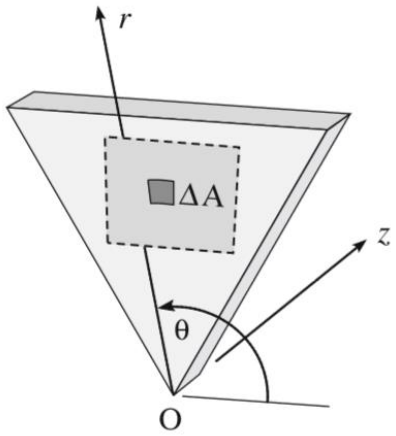

Fig. 4.1 Schematic of an outspread laser sheet appearing coordinate framework utilized in the text. Optics that structure the sheet are located at the source "O". The dashed square shape is the locale to be imaged by the camera, and the littler shaded area is the area DA in Eqs. 4.10 and 4.11 framed by anticipating DA over the width of the sheet (i.e., the whole degree of H(z)). Integrating Eqs. 4.7 and 4.8 over this volume gives the all out fluorescence. [39]

$$I_F(i,j) = \beta(i,j)\frac{F}{\Delta A} = \alpha(i,j)a(r,\theta)C \qquad \textbf{4.11}$$

Where b(i,j) is the portion of the absolute omnidirectional fluorescence received by the camera optics at a specific pixel area, and a(i,j) is the collection of concentration independent constants (with measurements of intensity per fixation)

$$\alpha(i,j) = \beta(i,j)\phi\epsilon P f(r) g(\theta) \qquad \textbf{4.12}$$

This allows an articulation for deciding C from estimated estimations of I_F to be composed as

$$C = [\alpha(i,j)a(r,\theta)]^{-1} I_F \qquad \textbf{4.13}$$

Where a(r,h) can be numerically coordinated for every individual image as indicated by the quick concentration field, and a(i,j) can be exactly decided, as examined **in Sect. 4.1.4**. Following Koochesfahani and Dimtakis (1985), Eqs. 4.9 and 4.13 can be discretized along any $\theta = \theta_0$, yielding

$$C(k,\theta_0) \approx [\alpha(r,\theta_0)]^{-1} I_F \prod_{n=1}^{k-1} exp\,[\epsilon C(n,\theta_0)\Delta r] \qquad \textbf{4.14}$$

Where the result of the exponentials results from the exponential of the total in Eq. 4.9. This task can be badly designed for PLIF applications with outspread laser sheets, since the polar joining along a beam way regularly depends on information from a cartesian image. Therefore, a(r,h) is frequently authorized to be near solidarity, through a blend of short beam

way lengths and additionally low concentrations. On the other hand, outspread pillar ways can be rendered parallel in the image locale by passing the incident beam through a large confocal lens [40] [41]. On the off chance that the fixation is uniform along the way, at that point Eqs. 4.4 and 4.7 lessen to

$$F(r_1) = I(r_0)\phi\epsilon C\exp(-\epsilon r C) \quad \textbf{4.15}$$

These relations grant trial assurance of e for a given dye (e.g., Walker 1987; Ferrier et al. 1993).

4.1.3 EXPERIMENTAL CONFIGURATIONS

4.1.3.1 Lasers

A PLIF framework requires an suitably matched laser and fluorescent dye mix, with at any rate some portion of the laser control within the assimilation band of the dye. Continuous wave (CW) argon-ion lasers working at 488 as well as 514.5 nm are utilized as the excitation source in roughly seventy five percent of watery PLIF tests announced in the fluid mechanics writing. Pulsed, frequency-doubled Nd:YAG lasers operating at 532 nm are utilized in the vast majority of the rest of the investigations, and their utilization has turned out to be progressively basic as of late. A couple of analyses have utilized copper vapor lasers [42] [43] and excimer lasers are some of the time used to instate photoactivatable (“confined”) dyes, however not for the excitation itself [44].

Particle lasers have the benefit of having prevalent bar quality and a nonstop yield that encourages flow visualization. At the point when worked in the TEM00 mode, particle lasers yield a shaft that is sensibly near a Gaussian crosssection, and when worked in a shut circle light-managed mode, have a steady power yield that simplifies alignment of the PLIF framework. By examination, Nd:YAG lasers have mediocre shaft quality and the power and conveyance of the pillar can shift from heartbeat to beat [45].

The fundamental preferred standpoint of Nd:YAG lasers is their powerful yield, commonly on the request of 107 W amid the pulse, rather than a constant yield of 10 W or less for a particle laser. Despite the fact that the pulse length of the Nd;YAG is only on the order of 10ns, the energy per picture presentation is normally a lot higher than that reachable with a particle laser, since the introduction time in the last case is constrained by important timescales in the flow. Incidentally, the high intensity of the Nd:YAG lasers can be risky. On

the off chance that the laser excitation power isn't little with respect to the immersion force of the dye, the frail excitation supposition (Sect. 4.1.2.1) is disregarded, bringing about a non-linear relationship among F and I. This impact can be significant with pulsed lasers, since short pulse times can lead to exceptionally high intensities, even when contrasted with those created by high-control CW lasers.

A CW laser working in the ideal TEM00 mode has a peak centerline intensity of 8P/pd2, where d is the beam diameter measured to the e-2 intensity contour. A run of the mill light sheet shaped by scanning a CW beam with a mirror has nearby local peak intensities of order 107 W/m^2 (e.g., [46]), with intensities several orders of size lower if a continuous sheet is framed by spreading the laser through a cylindrical lens. A commonplace light sheet shaped with a pulsed Nd:YAG laser has intensities of order 1011 W/m^2 (e.g., [47]). Estimations of I_{sat} have been assessed or deduced for both Rhodamine 6G and Rhodamine WT [48] to be of order 1010 W/m^2, which is significantly above the peak intensity for average particle lasers, however beneath that for pulsed lasers.

In any case, exact PLIF estimations can be made with excitation intensities over the weak excitation limit, in as much as the system is optically thin. In this situation, dye ingestion does not deliver varieties in I, and the non-straight connection among F and I winds up unsettled. Moreover, linearity among F and C has been shown to endure at high intensities for fluorescein, rhodamine WT, and rhodamine 6G, facilitating system calibration. An vital caveat is that two examinations show apparently irregular conduct when fluorescein is utilized with Nd:YAG lasers. The two examinations estimated an underlying increment in fluorescence along the bearing of the laser propagation in a uniform concentration of fluorescein, trailed by the expected decay. Further examinations are expected to decide whether this because of deviations from the Beer-Lambert law (dictated by legitimately estimating the laser intensity constriction) as well as due to fluorescence saturation effects.

4.1.3.2 Fluorescent dyes [39]

For fluid PLIF applications, the decision of fluorescent color is constrained to those that are in any event somewhat water solvent. The most widely recognized fluid PLIF colors are fluorescein and two rhodamine colors (rhodamine 6G, rhodamine B). These three xanthenes-class colors are all water dissolvable, with quantum efficiencies more prominent than 95%. Many dye properties reported in the literature (counting those for water soluble dyes) were estimated using ethanol as the dye solvent. Since properties, for example, absorption and

emission spectra, absorption coefficients, and diffusivities rely upon the decision of dissolvable ethanol-inferred property estimations parameters for the three most normal PLIF dyes in aqueous solutions. Fluorescein (a.k.a Uranine, disodium salt) is the most ordinarily utilized dye.

Fluorescein has top assimilation close to 490 nm (empowering efficient excitation with the 488 nm line of argon-particle laser), top outflow almost 510 nm, and has moderately low affectability to temperature changes. In any case, the assimilation spectra of fluorescein is emphatically pH-needy, with the end goal that retention (and consequently fluorescence) winds up irrelevant for pH4. This pH affectability can be misused for blending contemplates, as looked into later. Fluoresce in is known to be powerless to photobleaching (Saylor 1995; Crimaldi 1997), yet this issue has been appeared to be negligible for commonplace PLIF applications [49].

Table 2 Properties of three regular fluorescent dyes generally utilized for aqueous PLIF

Dye	$\lambda_{abs}\ (nm)$	$\lambda_{cm}\ (nm)$	$\varepsilon\ (cm\ M)^{-1}$	D (cm^2/s)	Percentage per °C
Fluorescein	490	515[a]	8.5E4[b] (488.0 nm)	5.1E-6[c]	-0.2[a]
Rhodamine 6G	525	555[d]	1.1E5[e] (514.5 nm)	1.2E-6[f]	
Rhodamine B	555	580[a]	8.6E4[a] (514.5 nm)	3.7E-6[c]	-1.8[g]

The table gives the peak absorption (λ_{abs}) and emission (λ_{em}) wavelengths, the absorption coefficient (e, as estimated at the wavelength given in parameters), the molecular diffusivity (D) at 20°C, and the fluorescence affectability to temperature estimated as percent change in fluorescence per °C near 20°C

4.1.3.3 Sheet optics

Sheet-shaping optics are utilized to change the laser beam into a sheet inside the flow. The sheet optics regularly live simply outside the flow apparatus, and the beam is conveyed there by means of either mirrors or a fiber optic cable. The most widely recognized methodology (Fig. 2a) for shaping a PLIF laser sheet utilizes a round and hollow focal point. A second methodology (Fig. 2b) utilizes a pivoting mirror to quickly examine the occurrence beam at

least multiple times over the image area. At times a turning polygon with mirrors on every aspect is quickly pivoted to such an extent that every feature delivers a solitary laser check.

Then again, a solitary mirror is incited by a galvanometer, which can be constrained by a simple voltage motion from a flag generator or a PC. Moving fluorescent features twisting in the subsequent PLIF image. The magnitude of the mutilation relies upon the proportion of the image integration time to an applicable advective timescale. The character of the distortion relies upon whether the image was made utilizing a cylindrical lens ("static sheet") or an examining mirror ("dynamic scan").

Numerical simulations of simplified situations are helpful to outline the two kinds of distortion (Fig. 3). The center board demonstrates a lot of five glorified filaments, each in the state of a +. Shift in weather conditions with speed u is from left to right, making the filaments advect a separation $\delta = ut_{exp}$ to the right during the PLIF image exposure time t_{exp}. The top board demonstrates a simulation of the subsequent PLIF image utilizing a static sheet. The image displays obscuring of highlights the advective way. This is a neighborhood bending that can be limited by requiring that

$$\Re_1 = \frac{\delta}{\lambda_s} \ll 1 \qquad \textbf{4.16}$$

Where λ_s is a length scale for neighborhood scalar filaments or features. For the simulation shown in Fig. 12, $\Re_1 = 4$ if λ_s is picked as the filament width (i.e., the width of the lines that structure the + , which are emphatically obscured), and < 1 = 0.3 if λ_s is picked as the element scale (i.e., the span of the + , which is sensibly very much imaged). Note that separations between features on inverse sides of the image are precisely represented.

By method of differentiation, a simulation of the PLIF image acquired with a dynamic sweep is shown in the lower panel, utilizing a similar advection velocity and image integration time as in the static case. Since small-scale features are uncovered just for the short duration which the high intensity laser beam disregards the comparing pixels, the local resolution is extremely sharp, with no noticeable obscuring. Be that as it may, the image shows twisting of the spatial connections between features isolated the advective way.

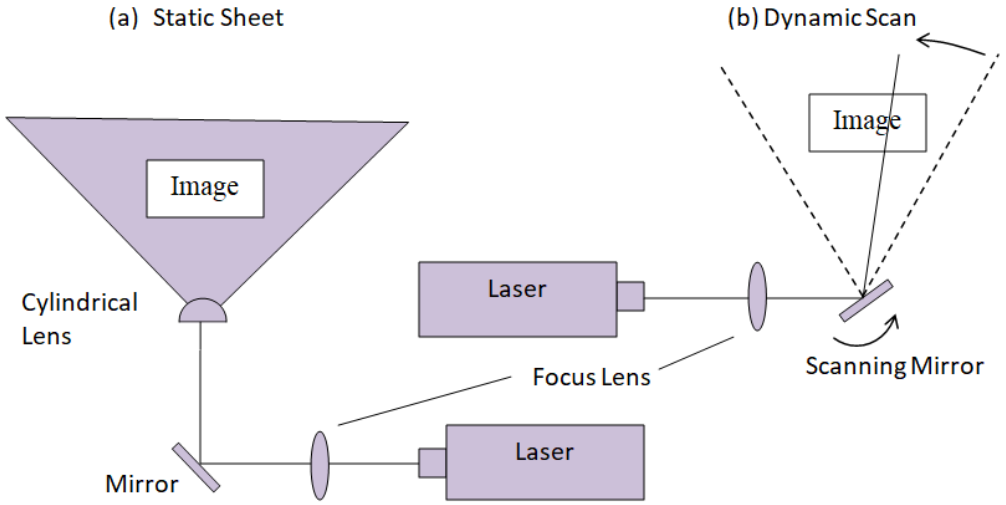

Fig. 4.2 Schematic for the optics utilized for the two most regular laser sheet types. Details of the focus lens are shown in Fig. 4 [39]

The flat separation between the + features is somewhat decreased with respect to their real division appeared in the center board. The separation is decreased on the grounds that the simulated dynamic scan is from ideal to left (against the advection). Had this been turned around, the separations would increment by an equivalent sum. This is a worldwide distortion that can be limited by requiring that

$$\Re_1 = \frac{\delta}{\lambda_s} \ll 1 \qquad \textbf{4.17}$$

Where L is the length of imaged area in the advective direction.

For the simulation Fig. 4.3, $\Re_2$ = 0.05, reliable with the little observed worldwide distortion. The < 2 disparity is ordinarily a lot simpler to fulfill in respect to the <1 imbalance, which presents favorable position to the dynamic output strategy when utilizing CW lasers, particularly in the event that one is keen on little scale conduct.

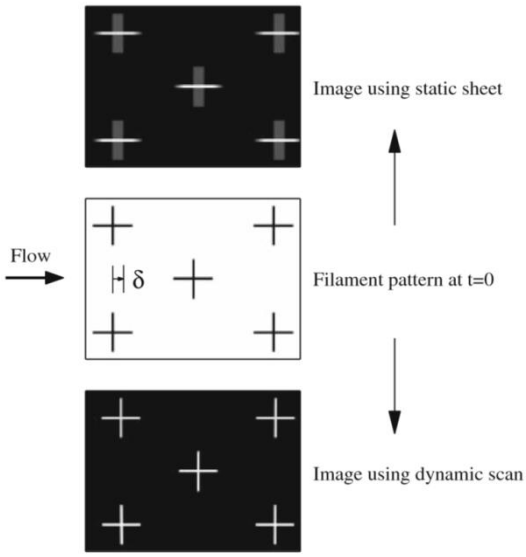

Fig. 4.3 Numerical simulations of bending coming about because of the two unique sorts of laser sheets appeared in Fig. 4.2. Advection is from left to right. The center board demonstrates the underlying position of five admired filaments (each in the state of a +). During the PLIF exposure interval t_{exp}, the filaments advect a separation d to one side. The upper and lower boards demonstrate the PLIF picture coming about because of a static sheet and a dynamic output, separately. The total exposure time and fluorescence is indistinguishable for each situation, however the idea of the advective bends is extraordinary, as talked about in the content [39]

4.1.3.4 Cameras

The decision of an advanced camera for a specific PLIF application is ordinarily an exchange off between expanding pixel tally, bit-profundity, and encircling rate. The pixel check influences spatial resolution, and ranges from as low as 256 x 256 (e.g., Van Vliet et al. 2004) to as high as 1,376 x 1024 (e.g., Brunchhanusen et al. 2005; Matsumoto et al. 2005). The bit-profundity decides intensity resolution N can resolve a limit of 2N discrete grayscales. Most of PLIF tests use 8-bit (e.g., Pan and Meng 2001; Matsumoto et al. 2005) cameras are utilized to catch a greater amount of the dynamic scope of concentrations in a system. The confining rate sets the greatest rate at which images can be gained (this rate may likewise be constrained by the system used to store the images). For rapid PLIF applications, surrounding rates as high as 955 frames for each second have utilized (Van Vliet et al. 2004).

A final thought is the otherworldly sensitivity of the camera. The senisitivity of the sCMOS chip at the wavelength of the fluorescence influences the required presentation time for a point is regularly justified for PLIF imaging (e.g., Crimaldi and Koseff 2001). Flatfield lenses are intended to concentrate on planar surfaces, even with a little profundity of field (large lens aperture). Most customary lenses have a spherical field characteristic, whereby the area of focused items is on a spiral curve from the sensor. Since laser light sheets are flat, and

constrained fluorescence flag regularly manages the utilization of large apertures, a flat-field lens can advance focal sharpness across the whole image.

4.1.4 IMAGE PROCESSING

Crude PLIF images caught by the camera should be post-processed for error rectification and adjustment. A powerful type of image processing includes the utilization of a foundation image of a uniform, realized focus to verifiably decide the constants α(i,j) defined in Eq. 4.12. The foundation concentration is additionally present during the real investigation. The depiction in this system is an extension of handling calculations utilized Koochesfahani and Dimotakis (1985), Prasad and Sreenivasan (1990), Catrakis and Dimotakis (1996), Borg et al. (2001), Crimaldi and Koseff (2001), and others. The dye fixation present in the n^{th} image are decayed as $C_n(i,j) = c_n(i,j) + b_n$, where b_n is the uniform foundation concentration present at the time the image was taken, and $c_n(i,j)$ is the concentration structure over the foundation (the ideal outcome). The constriction coefficient given by Eq. 4.9 at that point moves toward becoming $a(r,h) = a_c(r,h)\, a_b(r)$, where a_c and a_b are local attenuations due to c_n and b_n, separately. The fluorescence power (Eq. 4.11) in a image of just the uniform foundation is

$$B_n(i.j) = \alpha(i.j)a_b(r)b_n + D(i,j) \qquad \textbf{4.18}$$

Where D(i,j) is the dark-response of the camera. The dark response can be quantified as the normal of various images obtained with the lens cap secured, with the camera at average working temperatures. At the point when other dye notwithstanding the foundation is available, the recorded fluorescence intensity in the n^{th} image is

$$I_n(i,j) = \alpha(i,j)a_c(r,\theta)a_b(r)[c_n(i,j) + b_n] + D(i,j) \qquad \textbf{4.19}$$

Equations 4.18 and 4.19 can be consolidated to give an articulation for $c_n(i,j)$ that does exclude any express reference to a(i,j)

$$c_n(i,j) = \frac{b_n}{a_c(r,\theta)} \frac{I_n(i,j) - \left[a_c(r)\left(B_n(i,j) - D(i,j)\right) + D(i,j)\right]}{B_n(i,j) - D(i,j)} \qquad \textbf{4.20}$$

In the basic situation where $I_n \gg (B_n - D)$, Eq. 4.20 is precisely approximated by (noticing that $a_c(r)$ is structure solidarity for humble attenuations)

$$c_n(i,j) \approx \frac{b_n}{a_c(r,\theta)} \frac{I_n(i,j) - B_n(i,j)}{B_n(i,j) - D(i,j)} \qquad \textbf{4.21}$$

This estimation decouples the constriction adjustment $a_c(r)$ from the remainder of the image processing algorithm, permitting a step-wise correction scheme. To begin with, the crude images are flat-fielded through $(I_n - B_n) / (B_n - D)$ computation. Second, the images are scaled to dimensional units through increase by b_n. At long last, the subsequent images are adjusted for attenuation through division by $a_c(r,h)$, where $a_c(r,h)$ is determined from the dimensional, flat-fielded images using Eq. 4.9.

The requirement for Eq. 4.21 that $I_n \gg (B_n - D)$ can be in conflict with the longing to have $B_n - D$ itself sufficiently vast to keep away from discretization and noise errors out of sight image. This conflict is most effectively settled using a camera with a huge piece profundity. For instance, utilizing a 12-bit camera (dark scale esteems from 0 to 4,095) with run of the mill pixel estimations of $D = 50$, $B_n = 200$, $I_n = 2{,}000$, and $a(r,h) = 0.9$ the approximation error in Eq. 4.21 is less than 1%..

In Eq. 4.21, the dye concentration in the background image b_n must be known from the earlier. This can be cultivated either with a fluorometric estimation, or by an express portion count. As a rule, the foundation focus will change after some time because of option of extra dye during the investigation. For this situation, numerous foundation images are generally utilized, and image addition in time can be utilized for moderate images (Crimaldi and Koseff 2001). The alignment from pixel power to dimensional fixation should likewise be possible with an adjustment bend produced from various realized focuses blended in the test device (Karasso and Mungal 1996; Unger and Muzzio 1999). In lieu of utilizing the foundation image correction technique described by Eq. 4.21, it is conceivable to unequivocally address for certain blunders presented by the light sheet and imaging optics. A focal alignment picture can be utilized to address for focal point vignette (Ferrier et al. 1993), and geometrical contemplations can be utilized to compute and address for light sheet intensity variations (Diez et al. 2005). For a radial laser sheet produced with a mirror with steady output rate (see Fig. 4.1), the non-dimensional Cartesian intensity of the subsequent sheet is given by

$$I^*(x^*, y^*) = (x^{*2} + y^{*2})^{\frac{-1}{2}} \qquad \textbf{4.22}$$

Where x and y are standardized by y_0, the estimation of y at the base edge of the image, and I^* is the intensity distribution standardized by the reference power I ($x^* = 0$, $y^* = 1$). The subsequent sheet intensity alongside even and vertical profiles is appeared in Fig. 13. Laser sheets shaped with mirrors pivoting at non-uniform rates will create distinctive power

profiles. This methodology has been utilized to moderate spatial variations in concentrations (Webster et al. 2003), and to take out the horizontal intensity variation seen in Fig. 5 (Crimaldi and Koseff 2001).

Table 3 condenses basic wellsprings of mistake alongside conceivable remedies or potentially alleviations. In all cases, Eq. 4.22 rectifies just mistakes that are invariant in time, or whose variation (e.g., straight) is known between any pair of foundation images. Extra systems might be utilized for mistakes not redressed by Eq. 4.22. Specifically, a rectification for shot-to-shot varieties in laser power variation when utilizing pulsed lasers is ordinarily fundamental. This is normally done either by picking off a little segment of the laser power and estimating it with a power meter for each picture (Coolen et al. 1999), going the bar through a little cuvette with known concentrations and measuring the fluorescence [47]

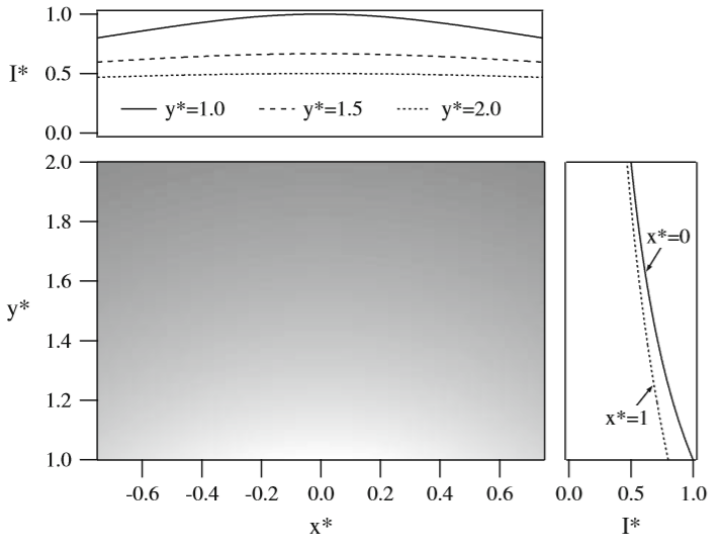

Fig. 4.4 Manufactured image of the non-dimensional intensity distribution of a laser sheet framed by a mirror pivoting at consistent angular rate (Eq. 4.22). The mirror is situated at (0,0). Likewise appeared flat and vertical profiles of the intensity. [39]

Table 3 Summary of error sources with corrections and/or mitigations

Category	Source	Correction	
		Equation 4.21	Other
Dye	Fluorescence from background dye	✓	
	Fluorescence sensitivity to pH and temperature	✓	
	Fluorescence saturation (strong excitation)	✓ [a]	
	Photobleaching		✓ [b]
Excitation	Spatial variation in light sheet (optics, etc.)	✓	
	Laser attenuation dye to background dye	✓	
	Laser attenuation due to instantaneous dye		✓ [c]
	Shot-to-shot laser power variation		✓ [d]
Optics	Refraction through walls or interfaces		✓ [e]
	Lens vignette	✓	
CCD	Pixel-to-pixel offsets (dark response)	✓	
	Pixel-to-pixel gain variations	✓	

Table adapted from [50]

[a] Just for optically thin solutions; see Sect. 4.1.3

[b] Not significant for most PLIF applications [49]

[c] Corrected via Eq. 4.14 or alleviated with low dye concentration and/ or potentially short pathlengths

[d] Typically moderated through closed-loop operation of CW lasers; see content for different adjustments

[e] Explicit remedy by means of lattice image [40]

5 MEASURING SET-UP AND RESULTS

5.1 EXPERIMENTAL SET-UP

Analyses were done at the Laboratory of Fluid Dynamics, Technical University of Liberec, in a horizontal circulating water channel with an closed test section (height 100 mm, width 100mm, length 2000 mm) shown in Fig. 5.2. A D = 4 mm diameter and L = 100 mm length circular cylinder was placed horizontally with its axis horizontal to the free stream velocity U shown in Fig. 5.1. The cylinder was heated electrically, kept at a constant temperature T_w with a potentiometer, and its temperature was measured by a thermocouple. Copper material is used so that conducting heat would be easier.

Measurements were carried out using PIV, enabling us to measure a two-dimensional cross-section of the flow field. The laser goes about as a photographic glimmer for the advanced camera, and the particles in the liquid disperse the light. Utilizing this technique, we can acquire the two-dimensional velocity distribution at various cases. From the velocity distribution streamlines can be resolved. From the velocity field v we can get the vorticity approximation $\varsigma = curl\,\mathrm{v}$ by numerical differentiation. The vorticity distribution demonstrates the exact area, centre, and the direction of rotation, enabling us to identify the structure of stream.

Fig. 5.1 Circular Cylinder (Material – Copper)

Measurements were completed at the three velocities of V = 0.003, 0.005, 0.007 m/s, corresponding to $Re_\infty = VD/\nu_\infty$ = 319, 479, 639 and at two cylinder temperature esteems (T_w = 291.5, 300.5 K). Here ν_∞ is the kinematic viscosity of the ambient air (at T_∞). The ambient temperature, and furthermore the temperature of the unheated cylinder, was $T_w = T_\infty = 291.5$ K.

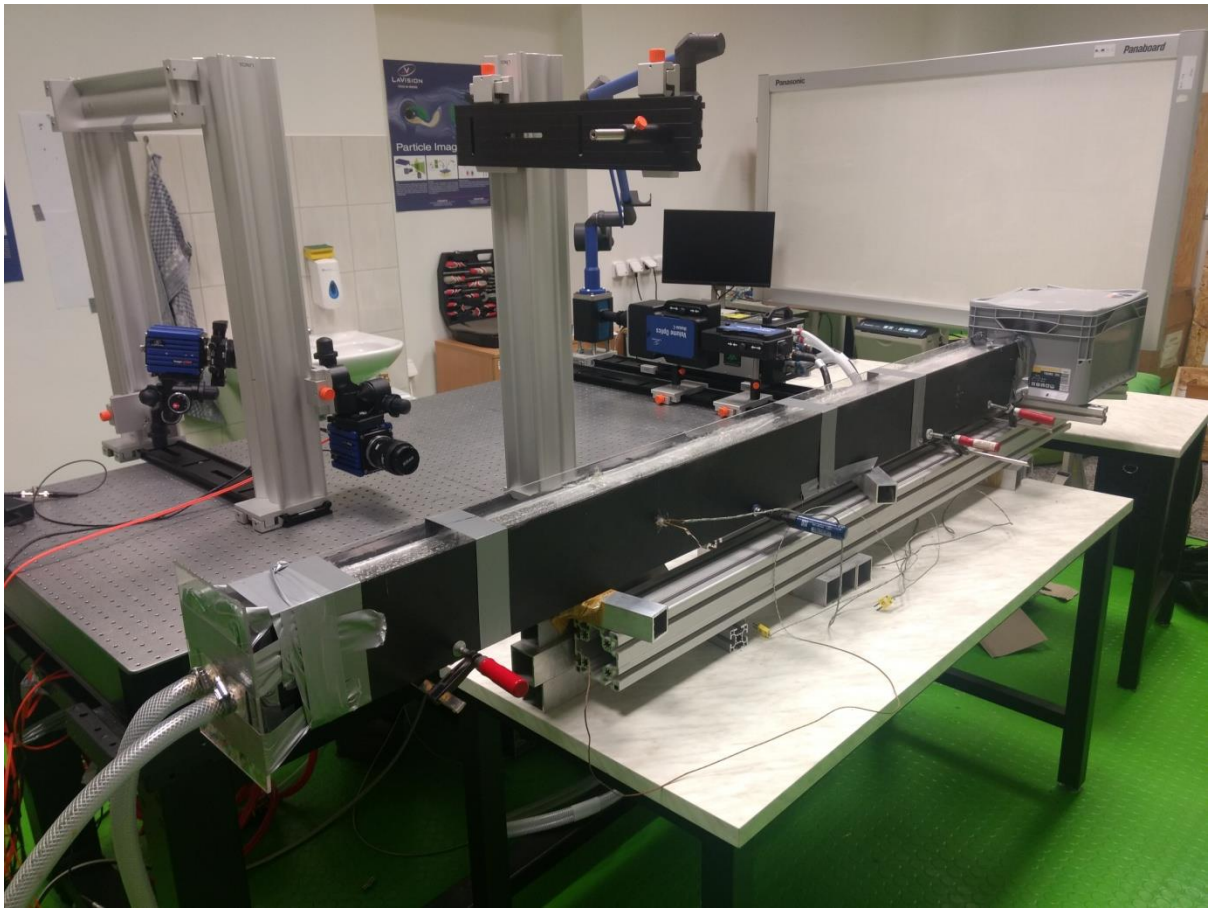

Fig. 5.2 Experimental set-up

For the heated cylinder, while ascertaining comparability numbers, M.N. Özisik [51] and Bejan [52] recommend putting together with respect to the average or film temperature of the cylinder and the ambient air

$$T_f = \frac{1}{2}(T_w + T_\infty) \qquad \textbf{5.1}$$

Here we characterize the reference temperature as

$$T_{ref} = T_\infty + c_{ref}(T_w - T_\infty) \qquad \textbf{5.2}$$

Which is reduced to Eq. 5.1 when $c_{ref} = c_f = 0.5$ where subscript f refers to the film esteem. The kinematic viscosity in relation to the reference temperature $\nu_{ref} = \nu(T_{ref})$ and the related Reynolds number $Re_{ref} = VD/\nu_{ref}$ – which considers likewise the cylinder temperature – can likewise be determined.

Table 4 Flow rate, Velocity and Reynolds number

Flow rate Q [l/min]	2	3	4
Flow rate Q [m^3/s]	3.33E-05	0.00005	6.67E-05
Velocity V [m/s]	0.0033	0.005	0.0067
Reynolds number at 18.5 °C	319	479	639
Reynolds number at 27.5 °C	395	592	789

Table 5 Viscosity – Temperature dependence

Temperature °C	**Temperature K**	**Dynamic Viscosity [mPa.s]**
18.5	291.5	1.0432
27.5	300.5	0.8446

Heating is done with means of a kanthal resistance wire of 0.8 mm. The resistance wire is as shown in Fig. 5.3. The Kanthal resistance wire is taped using insulation tape and inserted inside the hollow circular cylinder.

Fig. 5.3 Kanthal resistance wire

The current and voltage required for heating the Kanthal wire is provided by a triple DC power supply. Kanthal wire then conducts heat to the copper cylinder.

The heated cylinder temperature is measured with the help of thermocouple wires which is connected from the cylinder in the circulation channel to the DEWESoft software. The DEWESoft software helps in measuring the temperature and obtaining the temperature plots.

Fig. 5.4 Pump used for circulation of water

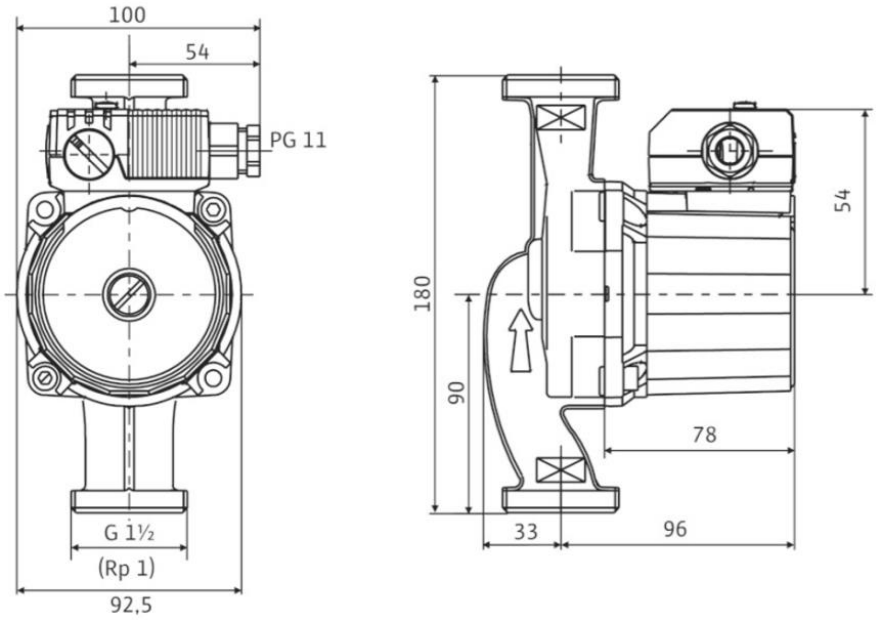

Fig. 5.5 Pump Drawing [53]

Pump Specifications

- Transport medium temperature -10 °C to +95 °C
- Mains connection 1~ 230 V, 50 Hz
- Enclosed class IPX2D
- Threaded connection Rp ½ , Rp 1
- Maximum operating pressure 10 bar

Since the pump capacity was higher a by-pass loop was introduced to reduce and control the water flow rate as shown in Fig. 5.6. The flow rate was controlled by a valve fitted in the pipeline. The water flow rate was checked with the help of a digital flow rate meter which displays the flow rate in litres/second.

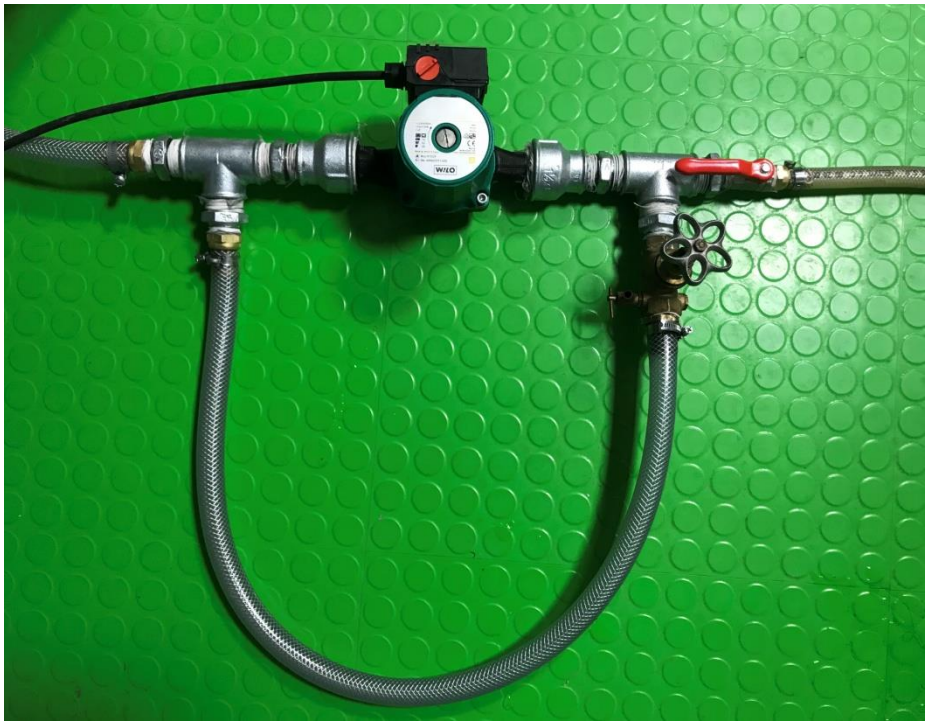

Fig. 5.6 Pump with a by-pass line

At the beginning calibration of set-up is done to have the lasers fall on the correct zone which is expected. The camera, laser and circulation channel is adjusted to perform the calibration and fixed at a position. The position of the set-up was not disturbed till the end of measurements and recordings.

Fig. 5.7 Digital Flow meter

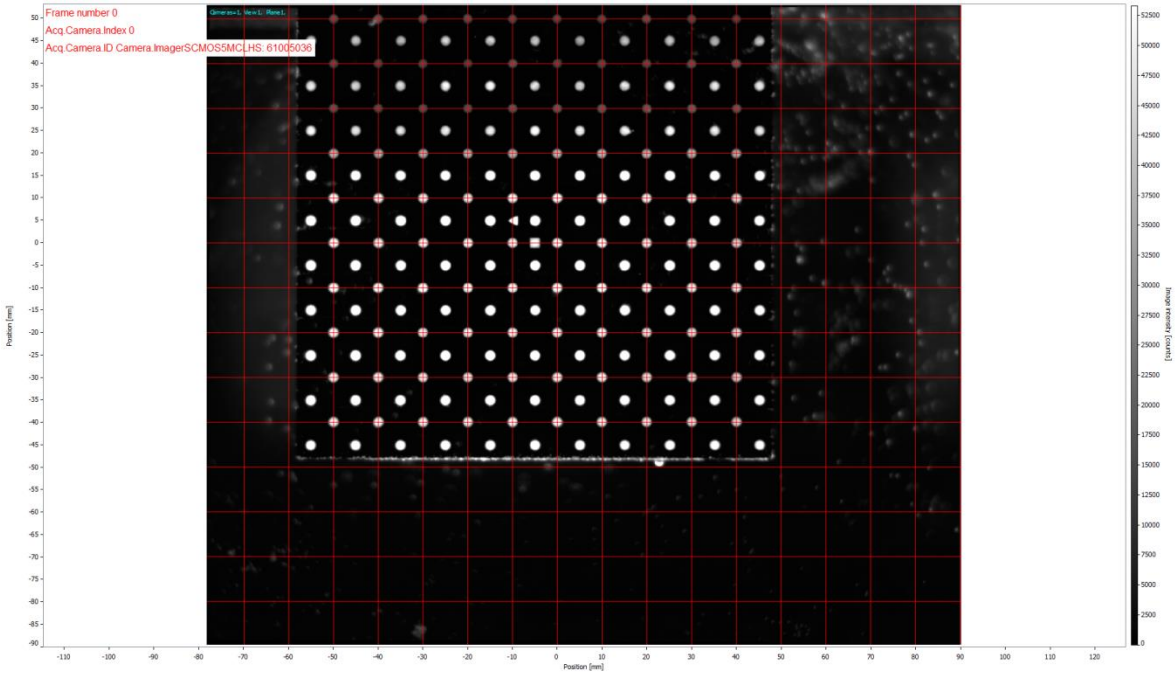

Fig. 5.8 Calibrated image

Before each investigation the tracer particles were suspended and consistently conveyed by mixing the circulation water channel. The examinations were begun in any event 2 min after these particles were included, permitting all fluid motions to soggy out. Although a large portion of the fluid movement disappeared amid this period still a fluid velocity could be distinguished. This fluid motion is by all accounts made by the temperature difference between the fluid inside the tank and the laboratory which give rise to the formation of small convection cells inside the channel. The subsequent velocity has a maximum magnitude of

about 0.5 mm/s. The spatial size of the observed motion is generally expansive and was seen to be of a similar request as the components of the test apparatus cross-area. Around 5 min before the real estimation began the heating was turned on permitting to settle the cylinder wall temperature. Because of this development the heat transfer coefficient changes bringing about a transiently lessening of the cylinder wall temperature. In this manner, the particle tracking measurements were begun after a steady temperature was achieved which took around a couple of minutes. The particles which are used in this experiment for flow visualization was Glass hollow spheres, 9-13 μm.

Before going into recording the Hardware connections are checked as shown in Fig. 5.10. The light source, timing unit, adapters and camera connections are checked. The recordings are done with control of the system for three flow rates 2 l/min, 3 l/min and 4 l/min. Each flow rates deals with two recordings one with heating the cylinder and the other without heating the cylinder.

A double-pulsed Nd:YAG laser is used, which can be bundled into thin light sheets for illuminating and recording the tracer particles

Laser Specifications:

- Flashlamp-pumped Nd:YAG
- Wavelength 532 nm
- Pockels cell
- Max. pulse energy typ. 100-200 mJ (up to 400 mJ)
- Max. frequency range typ. 15 Hz (up to 100 Hz)

Fig. 5.9 Double pulsed Nd:YAG laser

In the present examination, a spatial relationship system with interrogation window size of 64x64 pixels was utilized for the image processing to extricate velocity vectors. Figure demonstrates the resultant instantaneous velocity distribution with half overlap of the interrogation windows. The substitute shedding of the wake vortices at the opposite sides of the cylinder were uncovered obviously in the time grouping of the quick flow velocity disseminations, which is a average behavior of the wake flow behind an unheated cylinder at a Reynolds number of 639. A distribution zone directly behind the cylinder can be seen clearly in the ensemble-averaged velocity dissemination. The focal point of the distribution zone with most extreme upward flow velocity was observed to be at a downstream area of X/D ≈ 2.0.

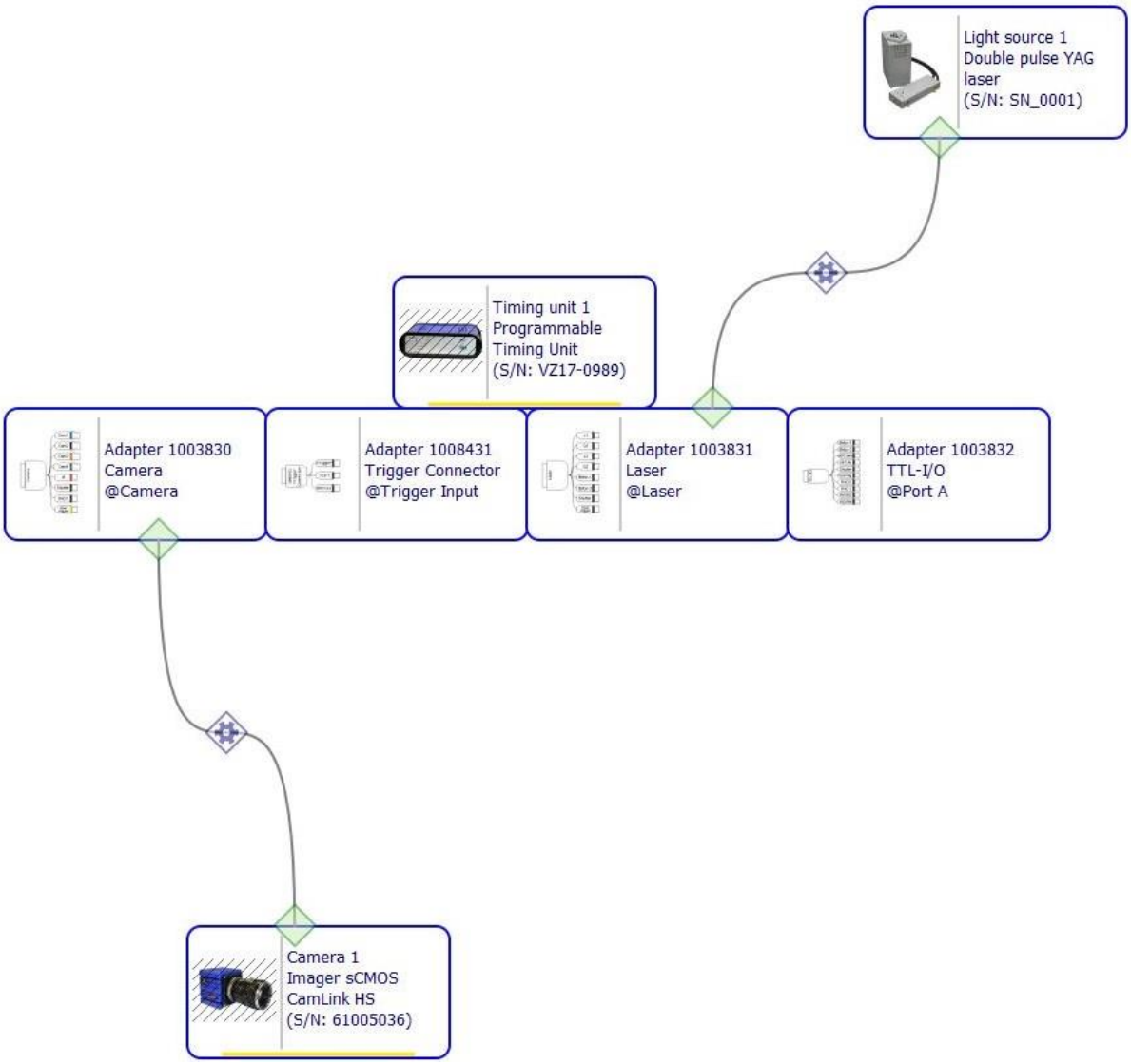

Fig. 5.10 Hardware Connections

Fig. 5.11 and Fig. 5.12 show a typical pair for the PIV measurements when the cylinder is heated and compared with unheated cylinder. The temperature of the heated cylinder was set to 27.5 °C.

PIV Measurement

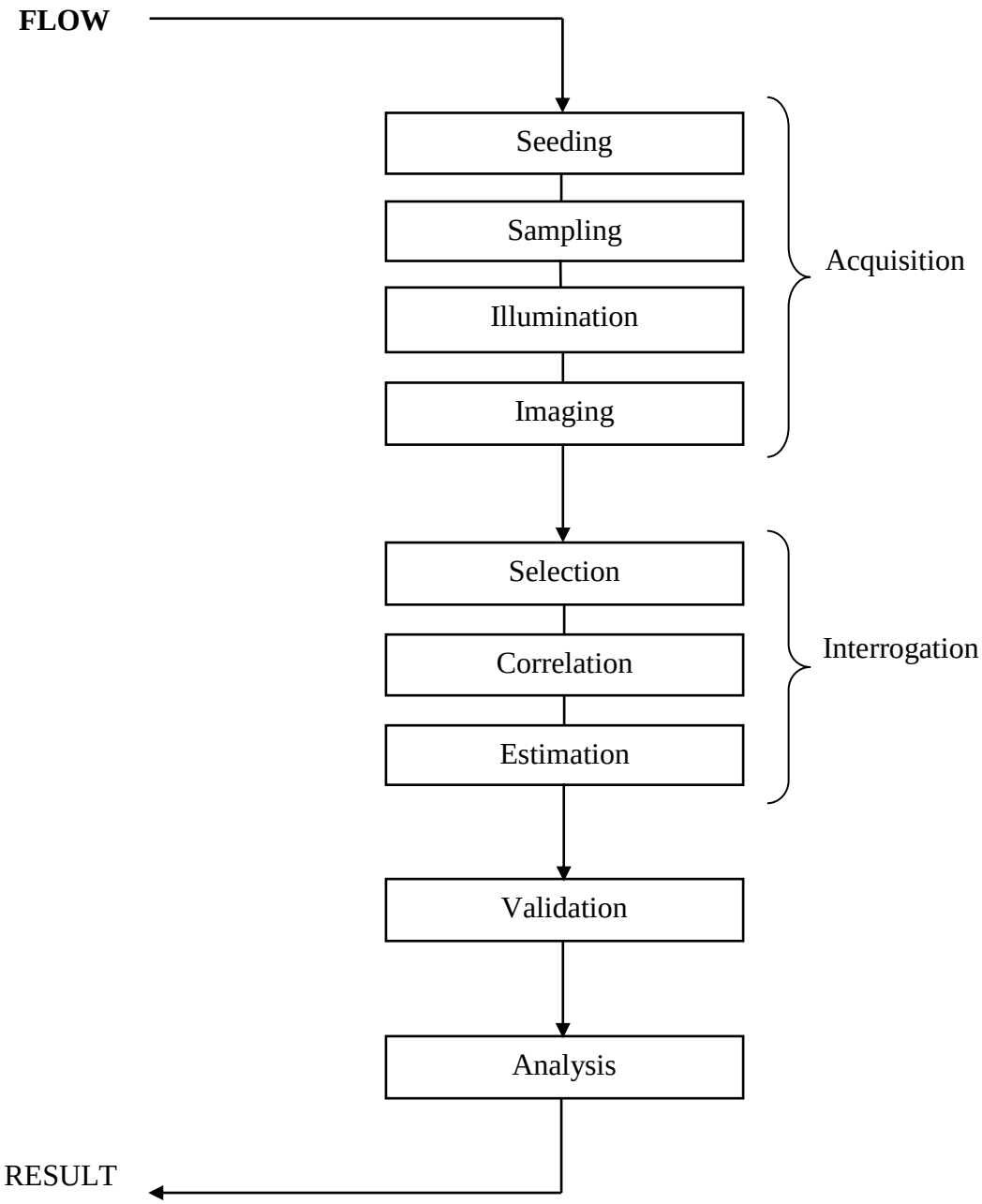

5.2 PIV RESULTS

5.2.1 AT FLOW RATE 2 l/min ~ CASE 1

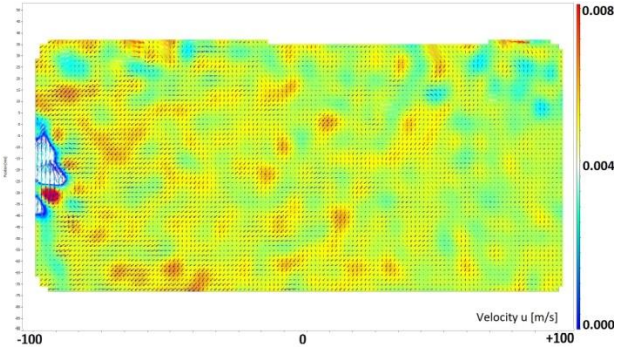

(a) Velocity u component [m/s] vs.distance [mm]

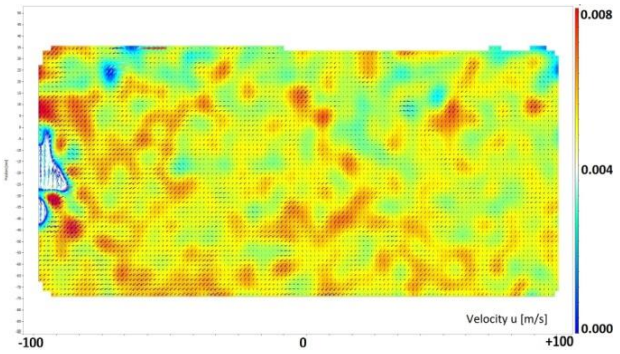

(a) Velocity u component [m/s] vs. distance [mm]

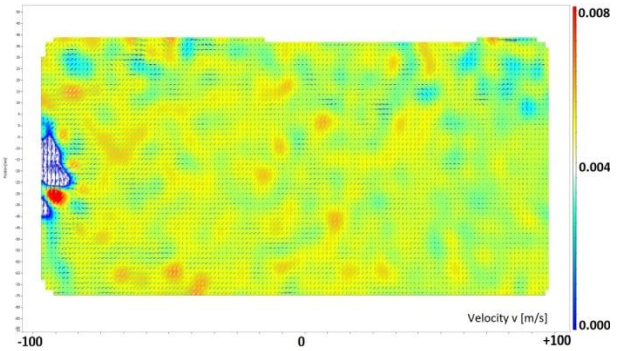

(b) Velocity v component [m/s] vs. distance [mm]

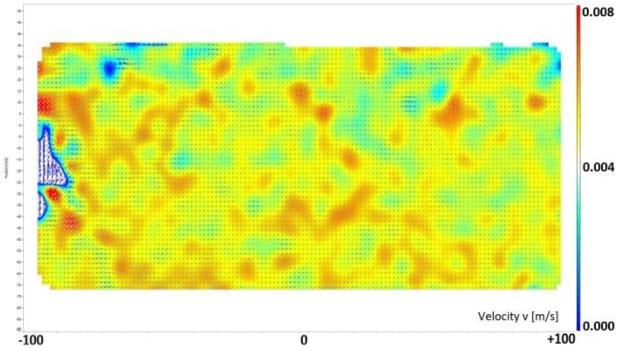

(b) Velocity v component [m/s] vs. distance [mm]

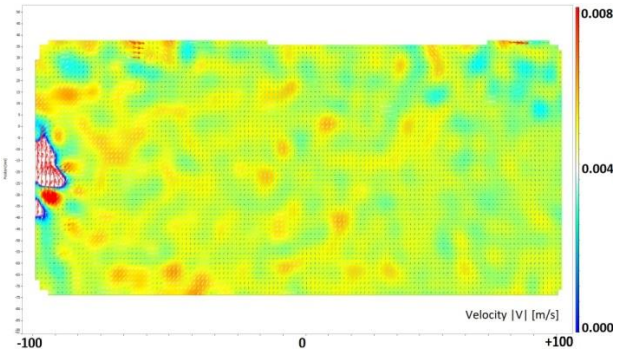

(c) Velocity - |V| [m/s] vs. distance [mm]

Fig. 5.11 PIV results at flow rate = 2 l/min for unheated cylinder

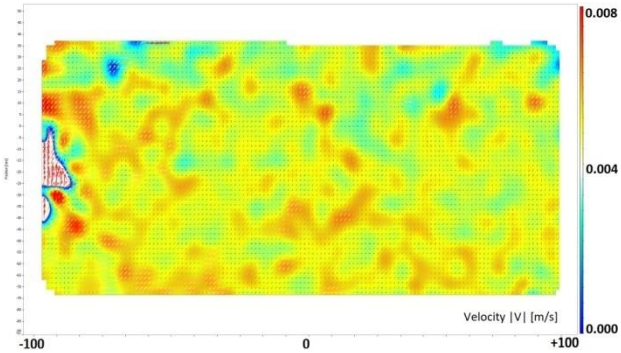

(c) Velocity - |V| [m/s] vs. distance [mm]

Fig. 5.12 PIV results at flow rate = 2 l/min for heated cylinders

Fig. 5.11 and Fig. 5.12 demonstrate a typical image pair for the PIV measurements when the cylinder was unheated and heated. The temperature of the heated cylinder was set to 27.5 °C. The resultant velocity vectors derived from the image pair are shown in fig. (c). The

instantaneous velocity vectors fields revealed more wake vortex shedding process and Karman vortex sheet formation in heated cylinder compared with unheated cylinder.

From Fig. 5.14 well defined thermally induced flow structures as “light clusters” can be identified in the wake behind the heated cylinder. The “light clusters” are actually the warm fluid shedding occasionally from the boundary layer around the heated cylinder. The Fig. 5.13 and Fig. 5.14 below depicts the Vorticity and Uncertainty of unheated and heated cylinders.

The normal and warmer molecules from the boundary layer around the unheated and heated cylinder would serve consequently as tracers to visualize the substitute shedding of the warm karman vortices in the wake of the heated cylinder.

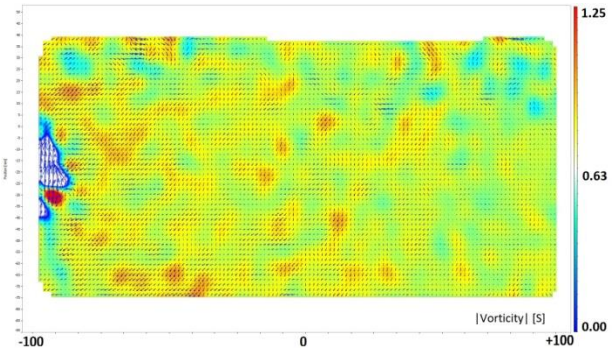

(a) Vorticity [S] vs. distance [mm]

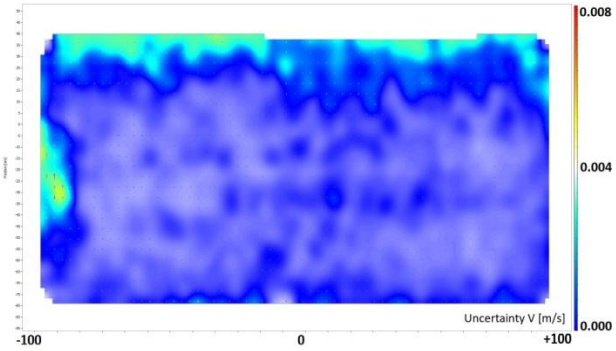

(b) Uncertainty V [m/s] vs. distance [mm]

Fig. 5.13 Vorticity and Uncertainty results for unheated cylinder at flow rate = 2 l/min

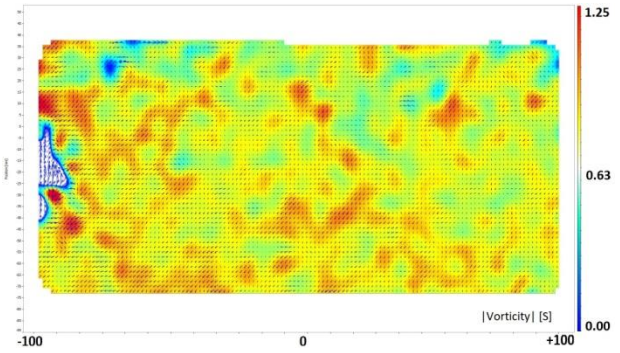

(a) Vorticity [S] vs. distance [mm]

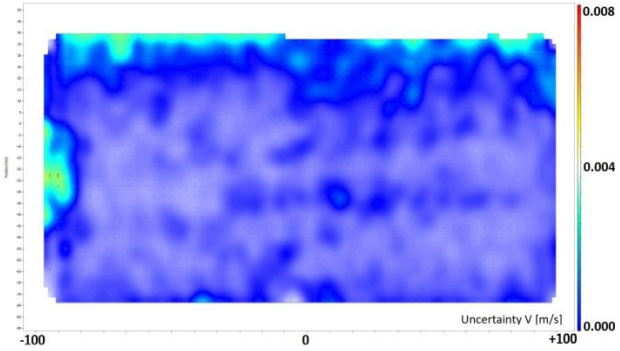

(b) Uncertainty V [m/s] vs. distance [mm]

Fig. 5.14 Vorticity and Uncertainty results for unheated cylinder at flow rate = 2 l/min

From the velocity vs. distance graph which is shown below Fig. 5.15 it was observed that velocity of heated cylinder is disturbed more when compared to velocity of unheated cylinder. This is due to formation of more vortex regions in heated cylinder than in unheated cylinder.

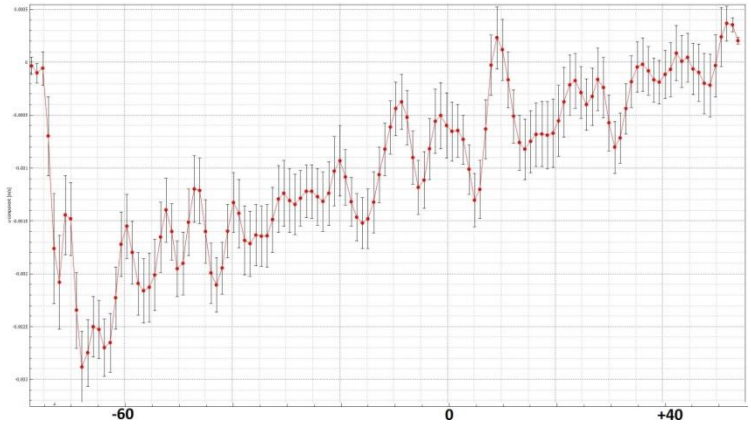

(a) u-component [m/s] vs. distance [mm]

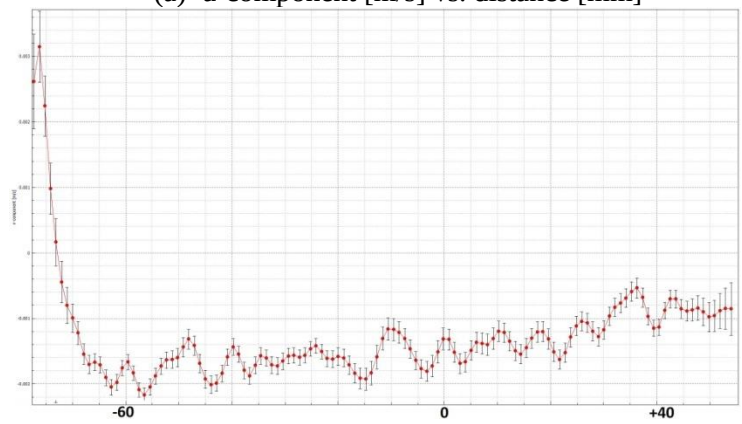

(b) v-component [m/s] vs. distance [mm]

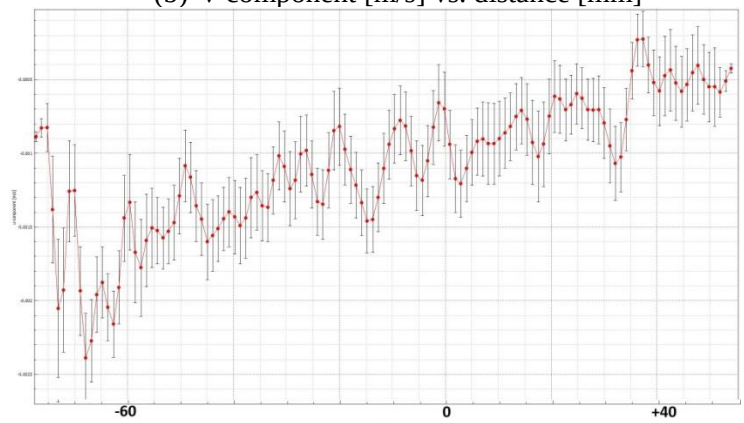

(c) u-component [m/s] vs. distance [mm]

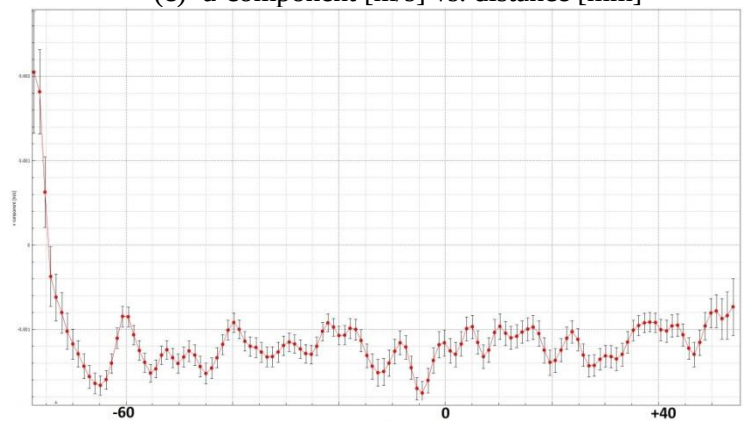

(d) v-component [m/s] vs. distance [mm]

Fig. 5.15 Graphs (a), (b) shows results for unheated cylinder and (c), (d) shows for heated cylinder

5.2.2 AT FLOW RATE 3 l/min ~ CASE 2

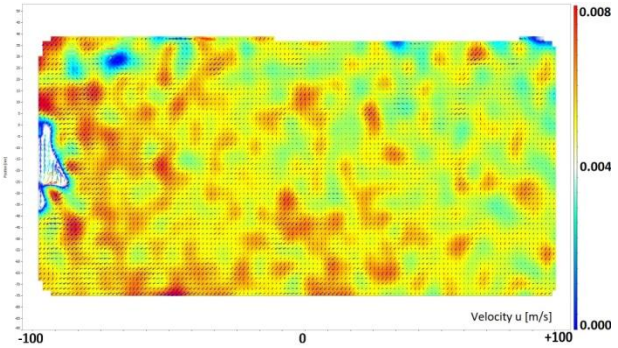

(a) Velocity u component [m/s] vs. distance [mm]

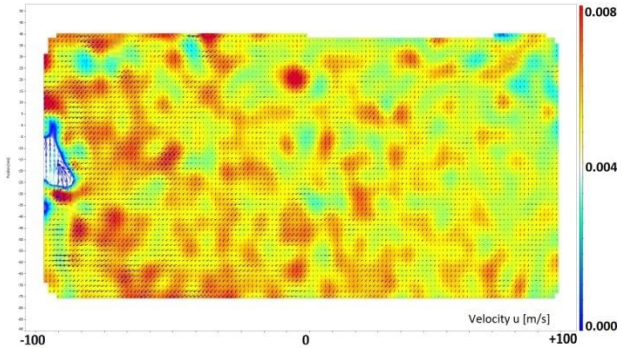

(a) Velocity u component [m/s] vs. distance[mm]

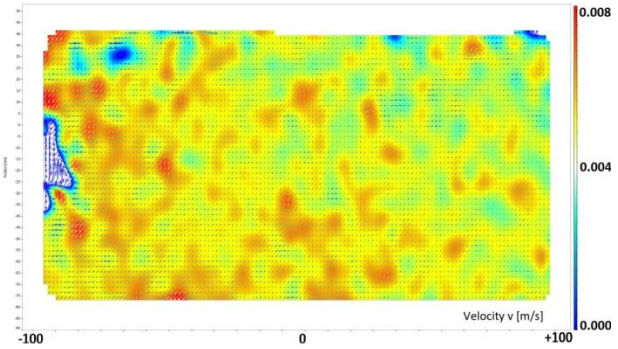

(b) Velocity v component [m/s] vs. distance [mm]

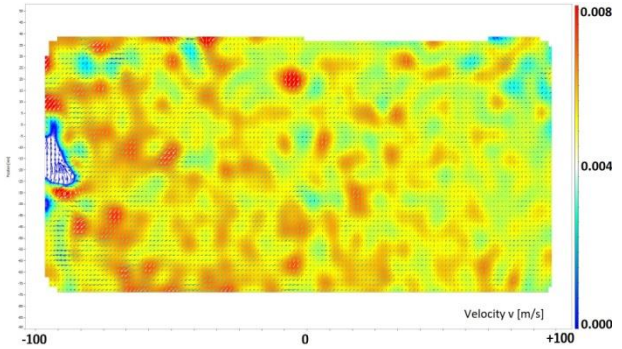

(b) Velocity v component [m/s] vs. distance[mm]

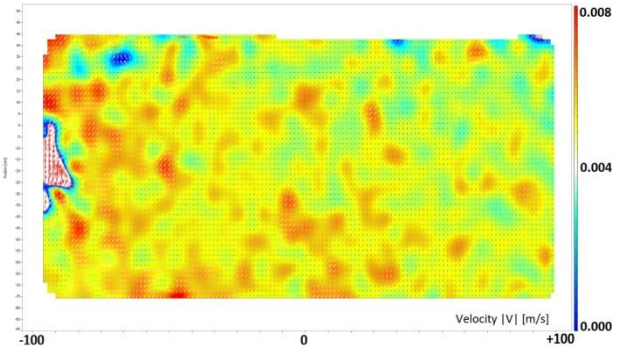

(c) Velocity - |V| [m/s] vs. distance [mm]

Fig. 5.16 PIV results at flow rate = 3 l/min for unheated cylinder

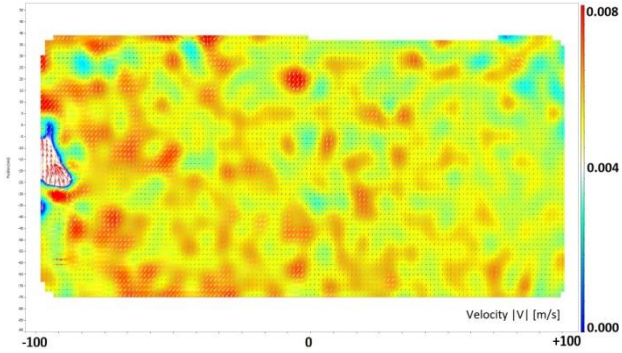

(c) Velocity - |V| [m/s] vs. distance [mm]

Fig. 5.17 PIV results at flow rate = 3 l/min for heated cylinders

The band-averaged velocity and temperature distributions were calculated based on instantaneous PIV measurements, and the results are shown in Fig. 5.11, Fig. 5.12, Fig. 5.16, Fig. 5.17. As described in Hu & Koochesfahani [10] a distribution zone behind the heated cylinder is uncovered in the ensemble-averaged velocity distribution which is like that found in the wake of the unheated cylinder Fig. 5.16, Fig. 5.16 and Fig. 5.21. The Images Fig. 5.18, Fig. 5.19 below shows the vorticity and uncertainty.

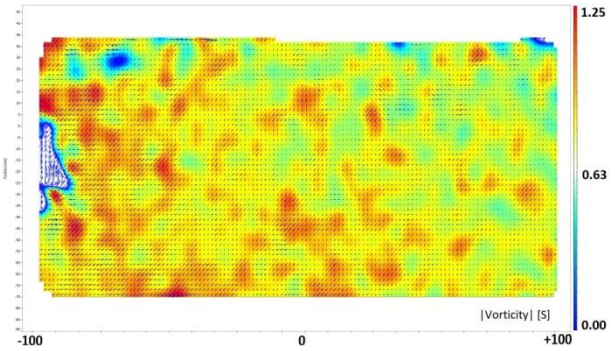

(a) Vorticity [S] vs. distance [mm]

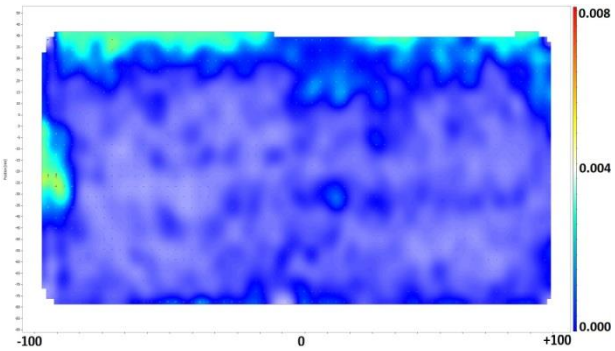

(b) Uncertainty V [m/s] vs. distance [mm]

Fig. 5.18 Vorticity and Uncertainty results for unheated cylinder at flow rate = 3 l/min

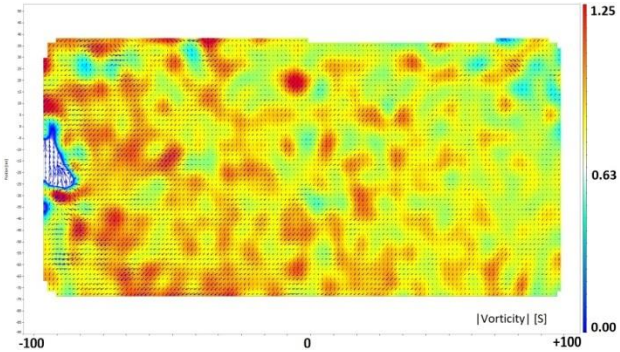

(a) Vorticity [S] vs. distance [mm]

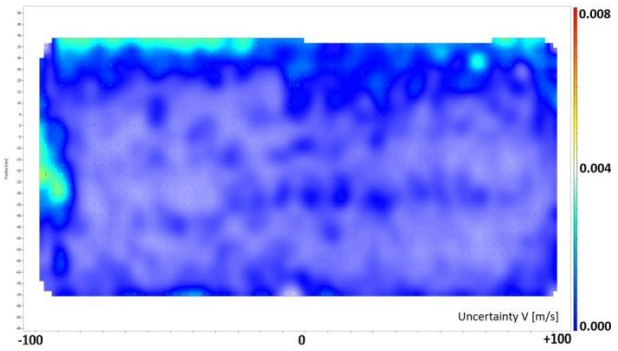

(b) Uncertainty V [m/s] vs. distance [mm]

Fig. 5.19 Vorticity and Uncertainty results for unheated cylinder at flow rate = 3 l/min

The recirculation zone for this case is found to turn out to be somewhat little contrasted and that in the wake of the unheated cylinder. The band-averaged temperature circulation uncovers that two high temperature districts exist at the opposite sides of the wake locale, relating to the shedding ways of the ‘karman’ vortices and the ‘warm blobs’ uncovered in the instantaneous measurement results.

The velocity vs. distance graph which is shown below Fig. 5.20Fig. 5.15 reveals a similar result as observed in case1, that the velocity of heated cylinder is disturbed more when compared to velocity of unheated cylinder. This is due to formation of more vortex regions in heated cylinder than in unheated cylinder.

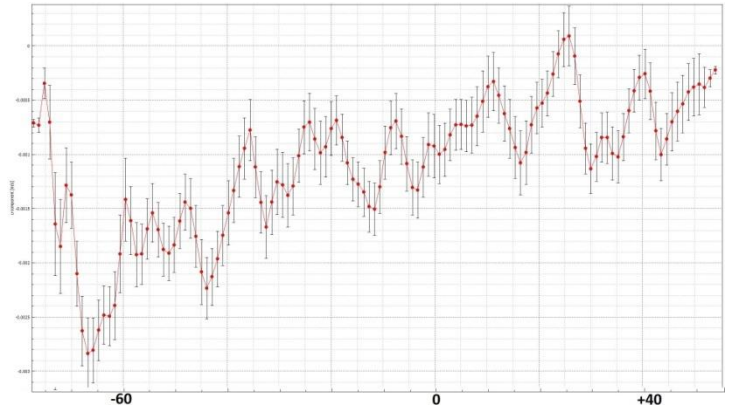

(a) u-component [m/s] vs. distance [mm]

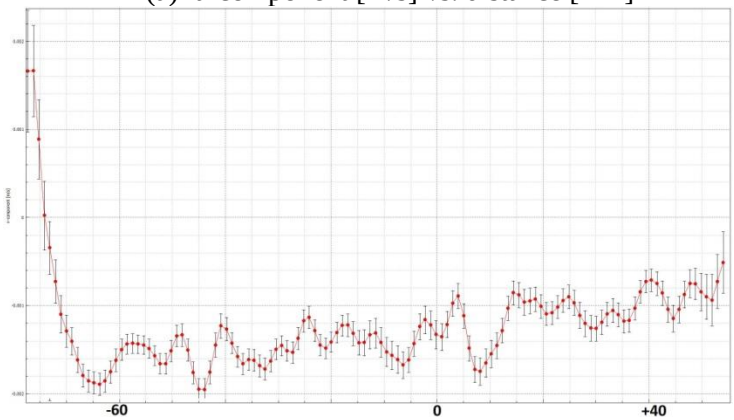

(b) v-component [m/s] vs. distance [mm]

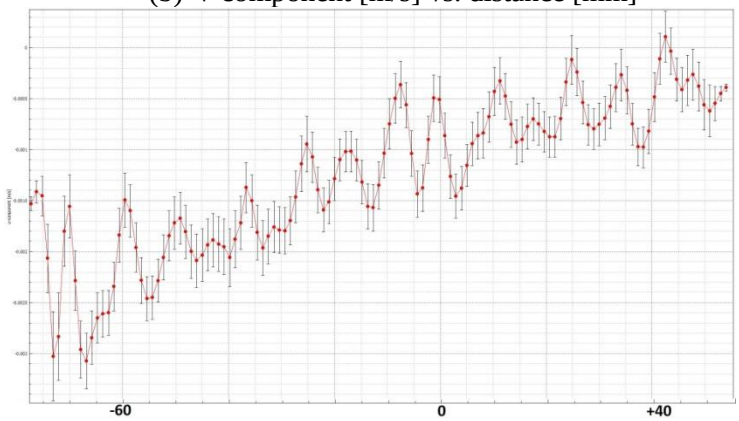

(c) u-component [m/s] vs. distance [mm]

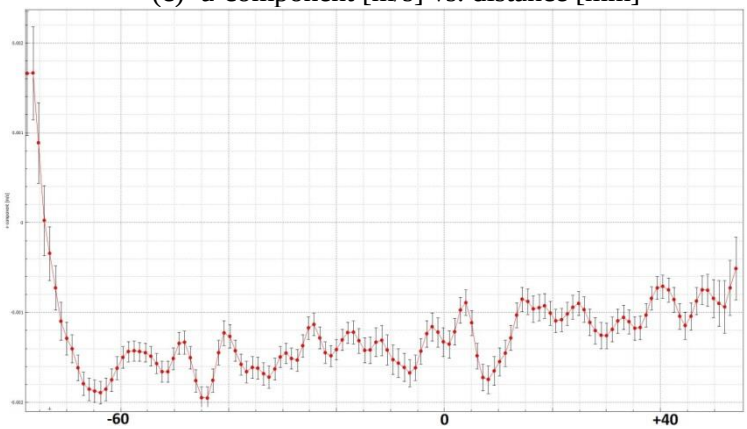

(d) v-component [m/s] vs. distance [mm]

Fig. 5.20 Graphs (a), (b) shows results for unheated cylinder and (c), (d) shows for heated cylinder

5.2.3 AT FLOW RATE 4 l/min ~ CASE 3

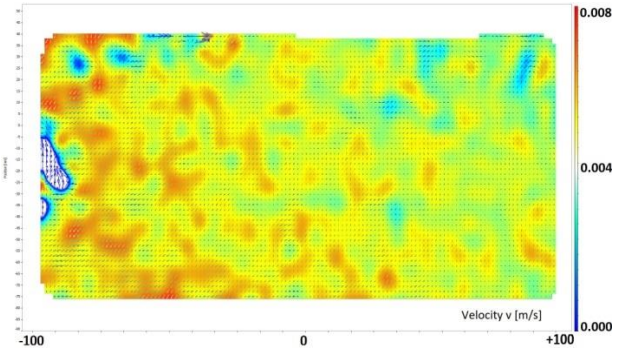

(a) Velocity u component [m/s] vs. distance [mm]

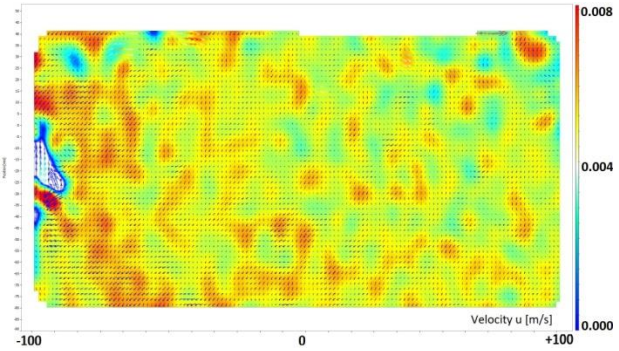

(a) Velocity u component [m/s] vs. distance [mm]

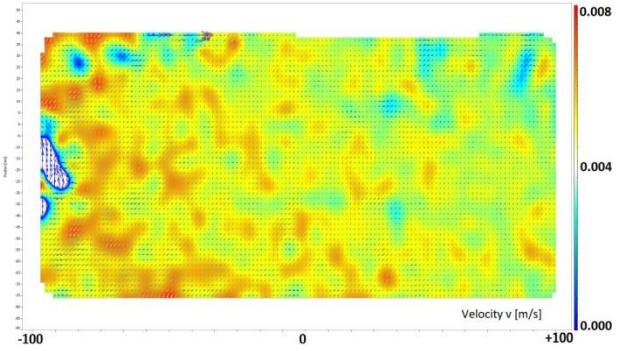

(b) Velocity v component [m/s] vs. distance [mm]

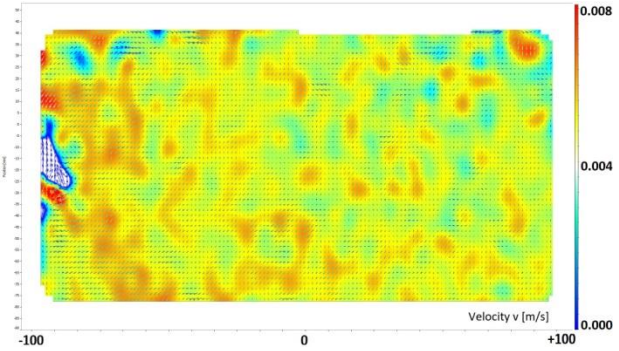

(b) Velocity v component [m/s] vs. distance [mm]

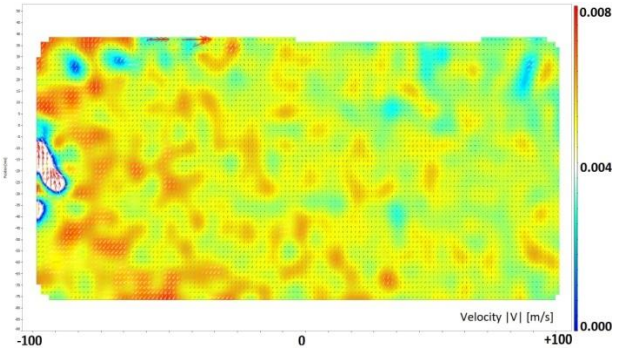

(c) Velocity - |V| [m/s] vs. distance [mm]

Fig. 5.21 PIV results at flow rate = 4 l/min for unheated cylinder

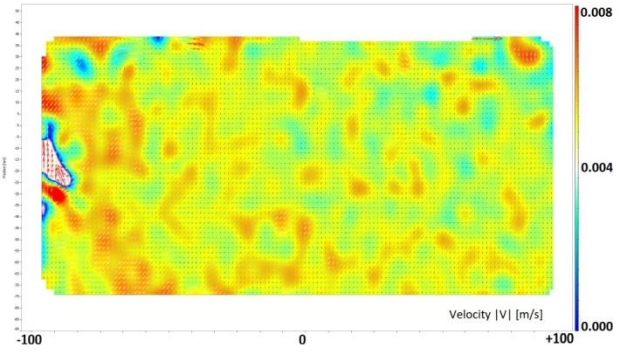

(c) Velocity - |V| [m/s] vs. distance [mm]

Fig. 5.22 PIV results at flow rate = 4 l/min for heated cylinders

Fig. 5.21 and Fig. 5.22 demonstrates a typical pair of images and the relating PIV measurement results in the wake of the unheated and heated cylinder for case 3, where the temperature of the cylinder was expanded to 27.5 °C (for example T_w = 27.5 °C). The instantaneous velocity field uncovered a shedding procedure of the wake vortices to shape a karman vortex road in the wake behind the heated cylinder is similar to that in the wake of the unheated cylinder (for example in Fig. 5.21). Compared with case 2, the 'light clusters' are significantly more articulated in the image attributable to the higher temperature of the

heated cylinder for this case. The instantaneous temperature distribution got from the image pair illustrates the substitute shedding of the heated cylinder to form 'warm blobs' occasionally at opposite sides of the heated cylinder.

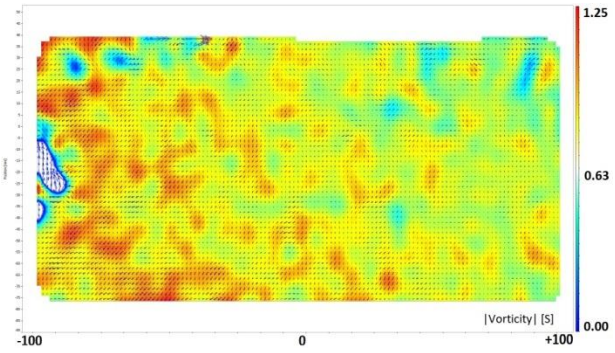

(a) Vorticity [S] vs. distance [mm]

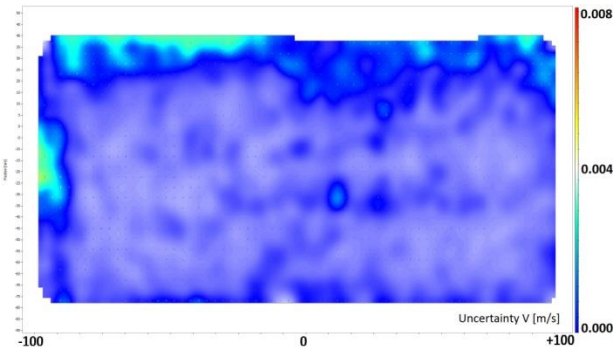

(b) Uncertainty V [m/s] vs. distance [mm]

Fig. 5.23 Vorticity and Uncertainty results for unheated cylinder at flow rate = 4 l/min

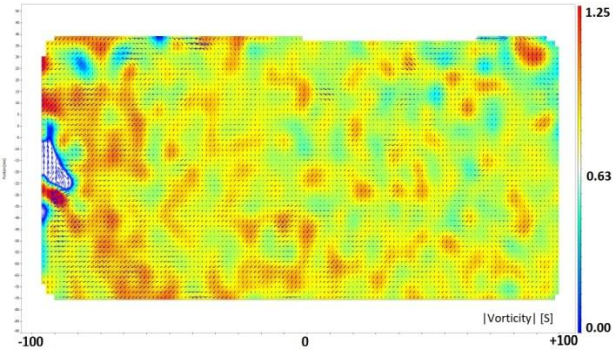

(a) Vorticity [S] vs. distance [mm]

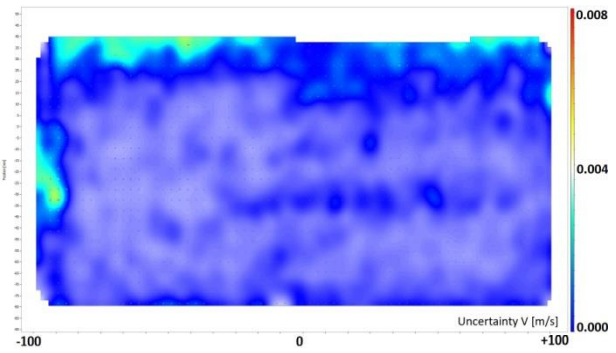

(b) Uncertainty V [m/s] vs. distance [mm]

Fig. 5.24 Vorticity and Uncertainty results for heated cylinder at flow rate = 4l/min

The length of the distribution zone in the group arrived at the band-averaged velocity distribution was observed to be nearly equivalent to that in the wake of the unheated cylinder (for example Fig. 5.21). While comparative temperature circulation examples can be found in the averaged temperature distributions for cases 2 and 3, a somewhat higher temperature was found in the wake of the heated cylinder for case 3 because of the higher flow rate of the channel in that case.

The band-averaged velocity and temperature dispersions uncovered that the wake flow design downstream of the cylinder turned out to be significantly not quite the same as those past cases. Rather than having a solid distribution zone right downstream of the cylinder, a long 'dead flow' zone with about zero velocity was observed to be situated in the close wake. A bigger and more grounded distribution zone was found to exist, yet further downstream, and its inside with most extreme upward velocity was situated at the downstream area X/D ≈ 6.0.

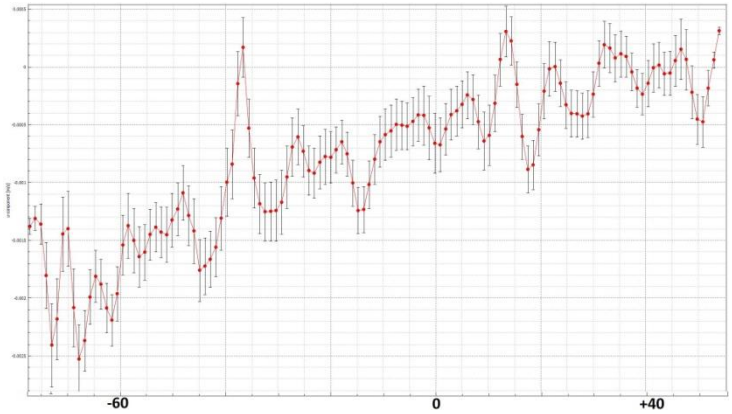

(a) u-component [m/s] vs. distance [mm]

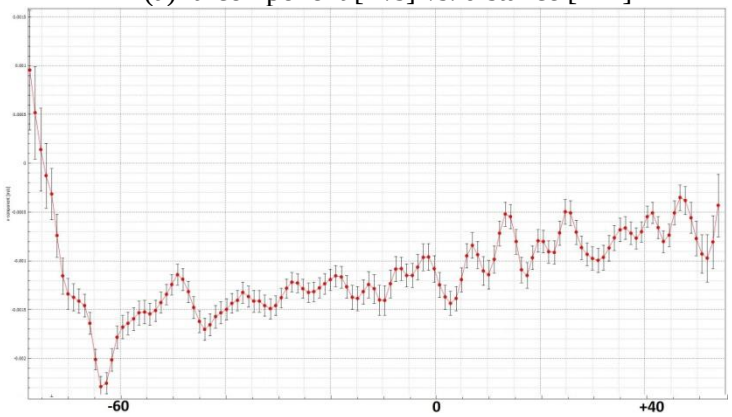

(b) v-component [m/s] vs. distance [mm]

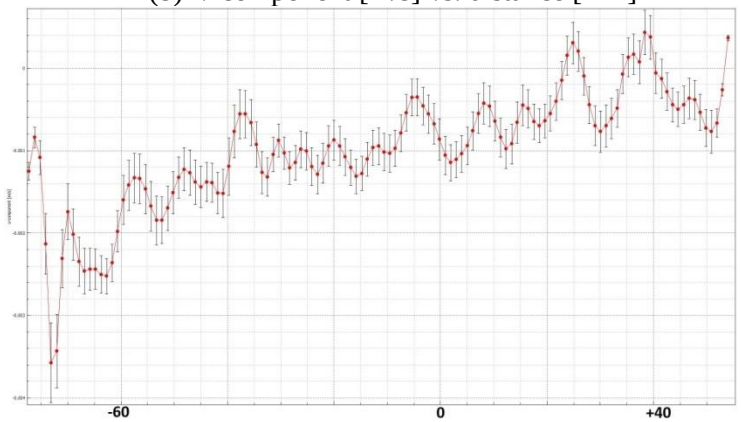

(c) u-component [m/s] vs. distance [mm]

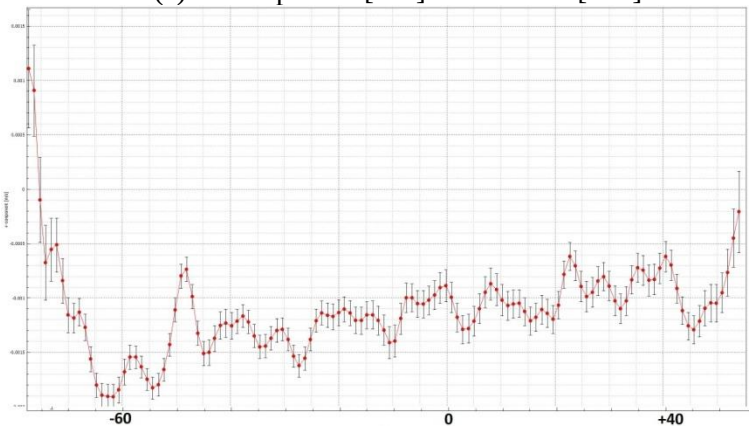

(d) v-component [m/s] vs. distance [mm]

Fig. 5.25 Graphs (a), (b) shows results for unheated cylinder and (c), (d) shows for heated cylinder

Significant contrasts likewise showed up in the mean temperature appropriation when contrasted with cases with small Richardson numbers. The heat wake (for example the regions with higher temperature) behind the heated cylinder was found to turn out to be a lot more extensive. The maximum instantaneous temperature difference in the wake became larger to 4 °C for this case. Since there is no synchronization, the results obtained show no proper vortices of the wake region and due to same reason the separation point couldn't be observed.

The velocity vs. distance graph as shown in Fig. 5.25 demonstrates a similar distribution of velocity over distance for both heated and unheated cylinder. This indicates at higher flow rates the velocity is similar irrespective of heated or unheated cylinder.

5.3 LIF RESULTS

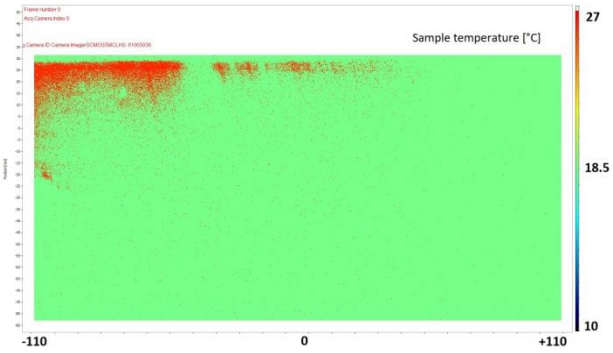

Fig. 5.26 LIF image for unheated cylinder at flow rate = 4 l/min

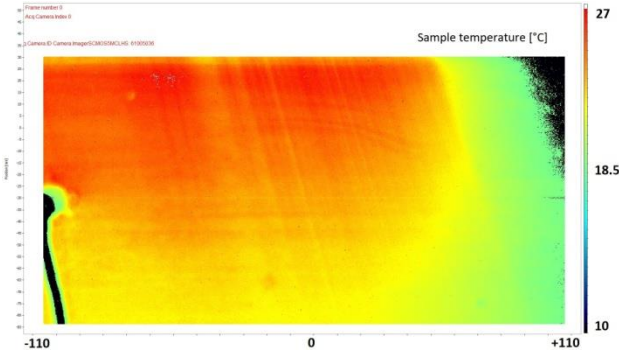

Fig. 5.27 LIF image for heated cylinder at flow rate = 4 l/min

The LIF measurements were taken at the flow rate of 4 l/min with heating and at normal temperature. Rhodamine 610 Chloride is used as fluorescent dye for flow visualization. The recordings for LIF is done in the same way as for PIV like before each investigation the fluorescent dye were suspended and consistently conveyed by mixing the circulation water channel. The examinations were begun in any event 2 min after these dye were added, permitting all fluid motions to soggy out.

And around 5 min before the real estimation began the heating was turned on permitting to settle the cylinder wall temperature. The Fig. 5.28 shows the temperature calibration where the initial temperature was 18.5 °C and final heated temperature was 27.5 °C. Because of this development the heat transfer coefficient changes bringing about a transiently lessening of

the cylinder wall temperature. In this manner, the Laser induced fluorescence measurements were begun after a steady temperature was achieved which took around a couple of minutes.

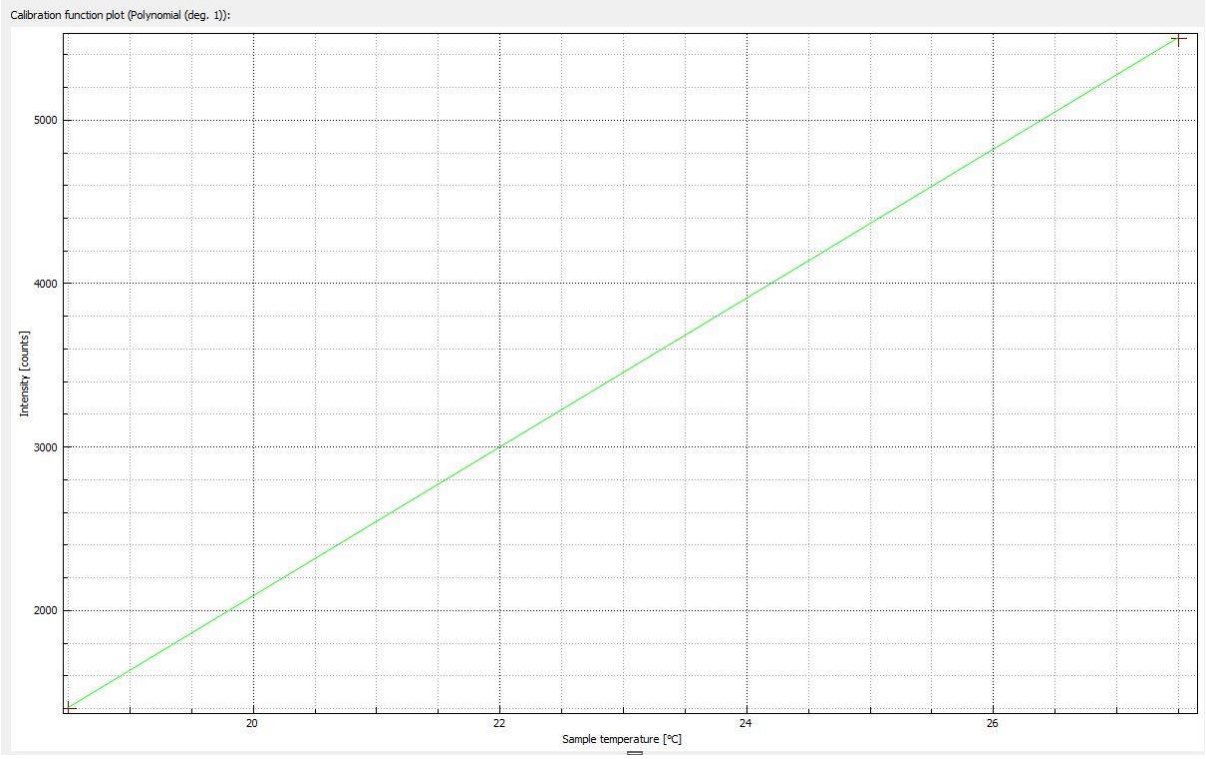

Fig. 5.28 Temperature Calibration

The dark regions uncovered in the LIF images featuring the warm limit layers. The temperatures indicated in Fig. 5.27 shows those areas are, therefore, highly averaged in spaces and underestimated in magnitude. The estimations become progressively dependable once the sizes of the flow structures become practically identical to the cylinder measurement after the shear layers move up, for example in the downstream locale of X/D > 1.5. The peak temperature in the focal point of the 'warm blob' at X/D ≈ 3.5 and X/D ≈ 5.5 was found to be ∼27.5 °C, or a most extreme instantaneous temperature differential of $(T_{max} - T_{\infty})$ = 9 °C in the wake behind the heated cylinder. It ought to be noticed that thermal structures with such temperature contrasts could in any case be uncovered with incredible detail in the LIF measurements inferable from the high temperature sensitivity of the fluorescent dye.

A resultant LIF estimation results are shown in Fig. 5.27, where the temperature of the heated cylinder was expanded to 27.5 °C. The vortex shedding process in the wake was found to turn out to be totally unique for this situation contrasted with every past case. Rather than an example of alternate shedding of the Karman vortices, the vortex structures and 'warm blobs' were found to shed simultaneously at the opposite sides of the heated cylinder, and their sizes

were marginally small. The 'dead flow' zone in the wake was seen to turn out be longer and more extensive. The vast distribution zone further downstream was additionally found to turn out to be longer and more extensive, with the focal point of the distribution zone moving further downstream to X/D ≈ 8.0. The mean temperature conveyance uncovered an area with high temperature close to the backside of the heated cylinder. The most extreme instantaneous temperature distinction in the wake flow was observed to be $\sim 4.5\ ^{\circ}C$.

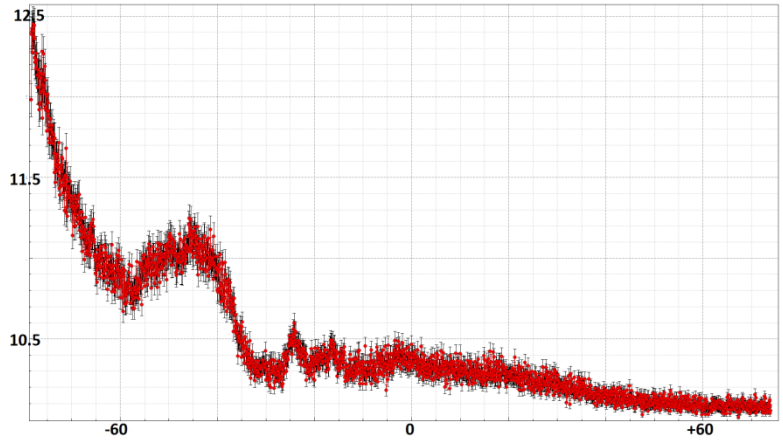

(a) Temperature [°C] vs. distance [mm]

(b) Temperature [°C] vs. distance [mm]

Fig. 5.29 Graphs (a), (b) shows results for unheated and heated cylinder

The simultaneous shedding of smaller vortex of the heated cylinder could be seen all the more unmistakably from the PIV and LIF measurements. These small wake vortex structures were noted to carry on increasingly like 'Kelvin-Helmholtz' structures than karman wake vortex structures. Examination of the time groupings of the prompt PIV estimation results uncovered that adjoining small vortex structures at each side of the heated cylinder would converge to shape bigger vortex structures or bigger 'warm blobs' in the region $5.0 \ll X/D \ll 7.0$.

The blending procedure was observed to be like the ‘matching’ procedure of ‘Kelvin-Helmholtz’ vortex structures in a free shear layer. The converging of the small vortices was seen to happen then again at opposite sides of the wake, which prompted the final exchange shedding of bigger karman vortex structures and ‘warm blobs’ further downstream.

Fig. 5.29 demonstrates the temperature distribution over distance for both heated and unheated cylinders where temperature of heated cylinder remains constant for a certain distance about 80 mm and then the temperature drops to normal temperature (i.e., 18.5 °C) and whereas in unheated cylinder there is temperature fluctuations at the beginning up to 40 mm and then it continues to remain at constant temperature.

6 CONCLUSION

The mechanism of the wake formation behind a heated cylinder has been investigated at a low Reynolds number and compared with the results of unheated cylinder. The experiment was conducted in a horizontal water channel with the heated cylinder placed horizontally at 135 cm away from the inlet and the forced flow approaching the cylinder in horizontal direction. By controlling the temperature of the heated cylinder, the corresponding Richardson number was varied between Ri = 0.0 (unheated) and Ri = 1.0 (heated), bringing out a difference in change of heat transfer from forced convection to mixed convection. Particle Image Velocimetry and Planar-Laser Induced Fluorescence methods was utilized to accomplish visualization for quantitative measurements of the velocity and temperature distributions in the wake behind the heated cylinder.

The measurements were done for three flow rates and observed that at low flow rates the wake distribution behind the heated cylinder is more when compared with unheated cylinder. And at high flow rates the instantaneous velocity vector fields reveals a similar wake vortex shedding process and Karman vortex sheet formation for both heated and unheated cylinder.

7 FUTURE WORK

The encouraging level of comparability observed opens the door to a number of future areas for investigation. Concerning these experimental results, the investigation for various temperatures of **heating** and **cooling** using **Stereo-PIV**, **Tomographic PIV** would be desirable to confirm the positive trend seen in this study with more focus on synchronization.

Furthermore, the reliable and detailed experimental data offers the opportunity to conduct a study of **Numerical simulation**. Computation of this case at varying Reynolds number would present a challenging test for current and future transition models.

REFERENCES

[1] R. J. Adrian, "Twenty years of particle image velocimetry," in *Experiments in Fluids*, 2005.

[2] K. Ohmi, A. Sapkota, and S. P. Panday, "2D and 3D PIV Experiments on the Wake of Two Tandem Circular Cylinders in a Cross Flow," *Proc. 7th KSME-JSME Therm. Fluids Eng. Conf.*, 2008.

[3] A. Schroeder and C. E. Willert, *Particle image velocimetry : new developments and recent applications*. 2008.

[4] A. Roshko, "On the Development of Turbulent Wakes from Vortex Streets," *Natl. Advis. Comm. Aeronaut. Washington, DC, United States*, 1954.

[5] E. Berger and R. Wille, "Periodic Flow Phenomena," *Annu. Rev. Fluid Mech.*, 2003.

[6] H. Oertel, "Wakes Behind Blunt Bodies," *Annu. Rev. Fluid Mech.*, 2002.

[7] c. Williamson, "Vortex Dynamics in the Cylinder Wake," *Annu. Rev. Fluid Mech.*, 2002.

[8] M. M. Zdravkovich, "Flow around circular cylinders, vol. 1. Fundamentals," *J. Fluid Mech.*, 1997.

[9] F. P. Incropera, D. P. DeWitt, T. L. Bergman, and A. S. Lavine, *Introduction to Conduction*. 2007.

[10] H. Hu and M. M. Koochesfahani, "Thermal effects on the wake of a heated circular cylinder operating in mixed convection regime," *J. Fluid Mech.*, 2011.

[11] "Drag of Blunt Bodies and Streamlined Bodies." [Online]. Available: https://www.princeton.edu/~asmits/Bicycle_web/blunt.html. [Accessed: 21-Apr-2019].

[12] "Drag Coefficient." [Online]. Available: https://en.wikipedia.org/wiki/Drag_coefficient#Blunt_and_streamlined_body_flows. [Accessed: 21-Apr-2019].

[13] Ravindra A. Shirsath, "Fundamentals of Airflow," 2016.

[14] R. J. Adrian, "Scattering particle characteristics and their effect on pulsed laser measurements of fluid flow: speckle velocimetry vs particle image velocimetry," *Appl. Opt.*, 2009.

[15] C. E. Willert and M. Gharib, "Digital particle image velocimetry," *Exp. Fluids*, 1991.

[16] J. Westerweel, "Digital Particle Image Velocimetry: Theory and Application," *Meas. Sci. Technol.*, 1997.

[17] I. Grant, "Particle image velocimetry: A review," *Proc. Inst. Mech. Eng. Part C J. Mech. Eng. Sci.*, 1997.

[18] N. Pedersen, *Experimental Investigation of Flow Structures in a Centrifugal Pump Impeller using Particle Image Velocimetry by*. 2000.

[19] M. Raffel, C. E. Willert, S. Wereley, and J. Kompenhans, *Particle Image Velocity A Practical Guide*. 2012.

[20] A. Melling, "Tracer particles and seeding for particle image velocimetry," *Meas. Sci. Technol.*, 1997.

[21] R. Mei, "Velocity fidelity of flow tracer particles," *Exp. Fluids*, 1996.

[22] A. T. Hjelmfelt and L. F. Mockros, "Motion of discrete particles in a turbulent fluid," *Appl. Sci. Res.*, 1966.

[23] E. W. North, R. R. Hood, S. Y. Chao, and L. P. Sanford, "Using a random displacement model to simulate turbulent particle motion in a baroclinic frontal zone: A new implementation scheme and model performance tests," *J. Mar. Syst.*, 2006.

[24] J. C. Agüí and J. Jiménez, "On the performance of particle tracking," *J. Fluid Mech.*, 1987.

[25] O. Akin and D. Rockwell, "Flow Structure in a Radial Flow Pumping System Using High-Image-Density Particle Image Velocimetry," *J. Fluids Eng.*, 2008.

[26] M. Stanislas and J. C. Monnier, "Practical aspects of image recording in particle image velocimetry," *Meas. Sci. Technol.*, 1997.

[27] R. Adrian, "Particle-Imaging Techniques For Experimental Fluid-Mechanics," *Annu. Rev. Fluid Mech.*, 2002.

[28] R. J. Adrian, "Dynamic ranges of velocity and spatial resolution of particle image velocimetry," *Meas. Sci. Technol.*, 1997.

[29] U. Ullum, J. J. Schmidt, P. S. Larsen, and D. R. McCluskey, "Statistical analysis and accuracy of PIV data," *J. Vis.*, 1998.

[30] H. Huang, D. Dabiri, and M. Gharib, "On errors of digital particle image velocimetry," *Meas. Sci. Technol.*, 1997.

[31] F. Scarano, "A super-resolution particle image velocimetry interrogation approach by means of velocity second derivatives correlation," *Meas. Sci. Technol.*, 2004.

[32] R. Theunissen, F. Scarano, and M. L. Riethmuller, "An adaptive sampling and windowing interrogation method in PIV," in *Measurement Science and Technology*, 2007.

[33] B. Wieneke, "PIV anisotropic denoising using uncertainty quantification," *Exp. Fluids*, 2017.

[34] A. Sciacchitano and B. Wieneke, "PIV uncertainty propagation," *Meas. Sci. Technol.*, 2016.

[35] LaVision, "Laser Induced Fluorescence." [Online]. Available: https://www.smart-piv.com/en/techniques/lif-plif/index.php. [Accessed: 03-Apr-2019].

[36] S. V. Patsayeva, V. I. Yuzhakov, and V. Varlamov, "<title>Laser-induced fluorescence saturation for binary mixtures of organic luminophores</title>," in *ICONO '98: Laser Spectroscopy and Optical Diagnostics: Novel Trends and*

Applications in Laser Chemistry, Biophysics, and Biomedicine, 2003.

[37] D. A. Walker, "A fluorescence technique for measurement of concentration in mixing liquids," *J. Phys. E.*, 1987.

[38] F. Lemoine, M. Wolff, and M. Lebouche, "Simultaneous concentration and velocity measurements using combined laser-induced fluorescence and laser Doppler velocimetry: Application to turbulent transport," *Exp. Fluids*, 1996.

[39] J. P. Crimaldi, "Planar laser induced fluorescence in aqueous flows," *Exp. Fluids*, 2008.

[40] A. J. Ferrier, D. R. Funk, and P. J. W. Roberts, "Application of optical techniques to the study of plumes in stratified fluids," *Dyn. Atmos. Ocean.*, 1993.

[41] E. Van Vliet, S. M. Van Bergen, J. J. Derksen, L. M. Portela, and H. E. A. Van Den Akker, "Time-resolved, 3D, laser-induced fluorescence measurements of fine-structure passive scalar mixing in a tubular reactor," *Exp. Fluids*, 2004.

[42] M. G. Mungal, "Instantaneous Three-Dimensional Concentration Measurements in the Self-Similar Region of a Round High-Schmidt-Number Jet," *J. Fluid Mech.*, 1994.

[43] P. S. Karasso and M. G. Mungal, "PLIF measurements in aqueous flows using the Nd: YAG laser," *Exp. Fluids*, 1997.

[44] L. Hansen, J. E. Guilkey, P. A. McMurtry, and J. C. Klewicki, "The use of photoactivatable fluorophores in the study of turbulent pipe mixing: Effects of inlet geometry," *Meas. Sci. Technol.*, 2000.

[45] A. W. K. Law and H. Wang, "Measurement of mixing processes with combined digital particle image velocimetry and planar laser induced fluorescence," *Exp. Therm. Fluid Sci.*, 2000.

[46] C. D. Troy and J. R. Koseff, "The generation and quantitative visualization of breaking internal waves," *Exp. Fluids*, 2005.

[47] J. W. Shan, D. B. Lang, and P. E. Dimotakis, "Scalar concentration measurements in liquid-phase flows with pulsed lasers," *Exp. Fluids*, 2004.

[48] L. A. Melton and C. W. Lipp, "Criteria for quantitative PLIF experiments using high-power lasers," *Experiments in Fluids*. 2003.

[49] L. G. Larsen and J. P. Crimaldi, "The effect of photobleaching on PLIF," *Exp. Fluids*, 2006.

[50] J. P. Crimaldi and J. R. Koseff, "High-resolution measurements of the spatial and temporal scalar structure of a turbulent plume," *Exp. Fluids*, 2001.

[51] M. N. Özisik, *Heat Transfer*. New York: McGraw Hill, 1985.

[52] A. Bejan, *Heat Transfer*. New York: John Wiley & Sons, 1993.

[53] "Wilo-Star-ST 25/7." [Online]. Available: https://wilo.com/de/de/. [Accessed: 26-Apr-2019].